Impact of Helix Characteristics on Slipstream Deformation in Propeller–Wing–Flap Interaction

Duivenvoorden, Ramon R.; Sinnige, Tomas; Veldhuis, Leo L.M.

DOI
10.2514/1.J064763

Publication date
2025

Document Version
Final published version

Published in
AIAA Journal

Citation (APA)
Duivenvoorden, R. R., Sinnige, T., & Veldhuis, L. L. M. (2025). Impact of Helix Characteristics on Slipstream Deformation in Propeller–Wing–Flap Interaction. *AIAA Journal*, *63*(11), 4798-4817. https://doi.org/10.2514/1.J064763

AIAA JOURNAL
Vol. 63, No. 11, November 2025

Impact of Helix Characteristics on Slipstream Deformation in Propeller–Wing–Flap Interaction

Ramon R. Duivenvoorden,* Tomas Sinnige,† and Leo L. M. Veldhuis‡
Delft University of Technology, 2629 HS Delft, The Netherlands

https://doi.org/10.2514/1.J064763

This paper explores the influence of the characteristics of the helical vortex system of a propeller slipstream on the resulting propeller–wing interaction, with a particular focus on how variations in helix angle impact slipstream deformation. Slipstream characteristics are changed by controlling the thrust and torque coefficient of the propeller through adjustments in blade pitch, advance ratio, and blade count. We conducted experimental measurements of a propeller–wing–flap model using seven-hole pressure probes, oil flow visualization, and infrared thermography in both cruise and high-lift configurations (with deployed slotted flap). The results presented in this paper demonstrate the dominance of the torque coefficient, and thereby longitudinal vorticity in the slipstream, on the slipstream deformation. The paper also underscores the role of the nacelle integration in the development of the slipstream, as well as the flow on the wing surface. The insights into the slipstream deformation provided in this work are essential for future closely coupled propeller–wing designs, particularly when it comes to high-lift configurations.

Nomenclature

c	=	chord, m
c_f	=	skin friction coefficient
$C_{p,t}$	=	total pressure coefficient, $(p_t - p_{s,\infty}/q_\infty)$
D	=	propeller diameter, m
h	=	heat transfer coefficient, $\mathrm{W}/(\mathrm{m}^2 \cdot \mathrm{K})$
J	=	advance ratio
k_f	=	thermal conductivity of fluid, W/mK
N_b	=	number of blades
p	=	pressure, Pa
$\dot{q}$	=	convective heat transfer, W/m^2
Q	=	torque, Nm
Q_c	=	torque coefficient, $Q/\rho V^2 D^3$
Q_c^*	=	equivalent torque coefficient calculated from probe measurements, $\iint (u\Delta v r^2/V_\infty^2 D^2)\,\mathrm{d}r\,\mathrm{d}\psi$
q_∞	=	freestream dynamic pressure, Pa
r, R	=	propeller radius, m
T	=	thrust, N
T_c	=	thrust coefficient, $(T/\rho V^2 D^2)$
T_c^*	=	equivalent thrust coefficient calculated from probe measurements, $\int ((C_{p,t} - 1)/2D^2)\,\mathrm{d}A$
T_W	=	wall temperature, K
T_∞	=	fluid temperature, K
u, v, w	=	velocity components, m/s
V_∞	=	freestream velocity, m/s
x, y, z	=	Cartesian coordinates, m
α	=	angle of attack, deg
$\beta_{0.7R}$	=	blade pitch angle at 70% radius, deg
δ_f	=	flap deflection, deg
ν	=	kinematic viscosity, m^2/s
ρ	=	density, kg/m^3
ψ	=	azimuthal angle, deg

Received 21 August 2024; accepted for publication 21 April 2025; published online 11 July 2025.

*Ph.D. Candidate, Faculty of Aerospace Engineering, Department of Flow Physics and Technology; Cluster of Excellence SE^{2}A–Sustainable and Energy-Efficient Aviation, Technical University of Braunschweig, 38108 Braunschweig, Germany; r.r.duivenvoorden@tudelft.nl.

†Assistant Professor, Faculty of Aerospace Engineering, Department of Flow Physics and Technology; Cluster of Excellence SE^{2}A–Sustainable and Energy-Efficient Aviation, Technical University of Braunschweig, 38108 Braunschweig, Germany; t.sinnige@tudelft.nl.

‡Full Professor, Faculty of Aerospace Engineering, Department of Flow Physics and Technology; l.l.m.veldhuis@tudelft.nl.

I. Introduction

PROPELLER–WING aerodynamic interaction is a critical factor in the performance of modern propeller-driven aircraft. As aircraft designs continue to evolve, particularly with the increasing interest in distributed propulsion systems and other advanced propeller–airframe integration concepts, understanding the slipstream deformation and development resulting from the propeller–wing aerodynamic interaction is paramount. Foundational works on the propeller–wing aerodynamic interaction by, among others, Witkowski [1], Jameson [2], and Veldhuis [3] have already established the basic principles of the interaction. More recently, the topic has been expanded upon by Sinnige [4], van Arnhem [5], and de Vries [6]. However, while the propeller–wing aerodynamic interaction is well-defined in terms of impact on performance characteristics, insight into the actual flow development is seldom provided. Furthermore, understanding of the high-lift condition is significantly lagging behind that of the cruise condition, owing to its additional complexity and dependency on viscous interactions. Considering the renewed interest in distributed propellers and high-lift propeller systems, understanding the propeller–wing aerodynamic interaction in high-lift conditions is essential.

Felli [7] provides a fundamental analysis of the mechanisms behind propeller–wing aerodynamic interaction. He shows that the slipstream deformation is dominated by the physical interaction of the slipstream vortical helix with the wing. This induces vortex image effects, as well as spanwise pressure gradients, that displace vortices as they stretch along the wing surface and deform the slipstream. The vortex imaging effect applies to two main interactions: the image of the streamwise component of vorticity in the wing surface and the image of the tip vortices in the leading edge. They are illustrated in Fig. 1. The spanwise pressure gradient effect relates to spanwise crossflow induced on the slipstream edge as a result of a static pressure difference inside and outside the slipstream. For the symmetrical, nonlifting wing, we can identify three main contributions: scaling of the local pressure due to increased dynamic pressure in the slipstream, the angle of attack induced by the tangential velocities in the slipstream, and the local static pressure field behind the propeller. For a lifting wing, however, the pressure distribution around the wing changes both inside and outside the propeller slipstream. The various contributions are illustrated in Fig. 2. Note that the impact of angle of attack also changes the sign of the effect of dynamic pressure scaling. The direction of the induced crossflow due to the spanwise pressure gradients can

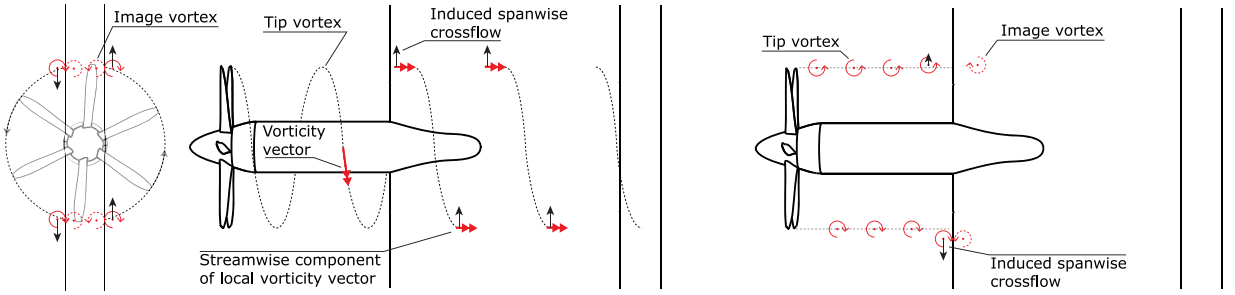

a) Effect of the vortex images of the local streamwise vorticity component over the wing surface

b) Effect of the tip vortex image in the wing leading edge

Fig. 1 Schematic illustration of the image vortex effects of the slipstream vorticity in the wing leading edge and over the surface.

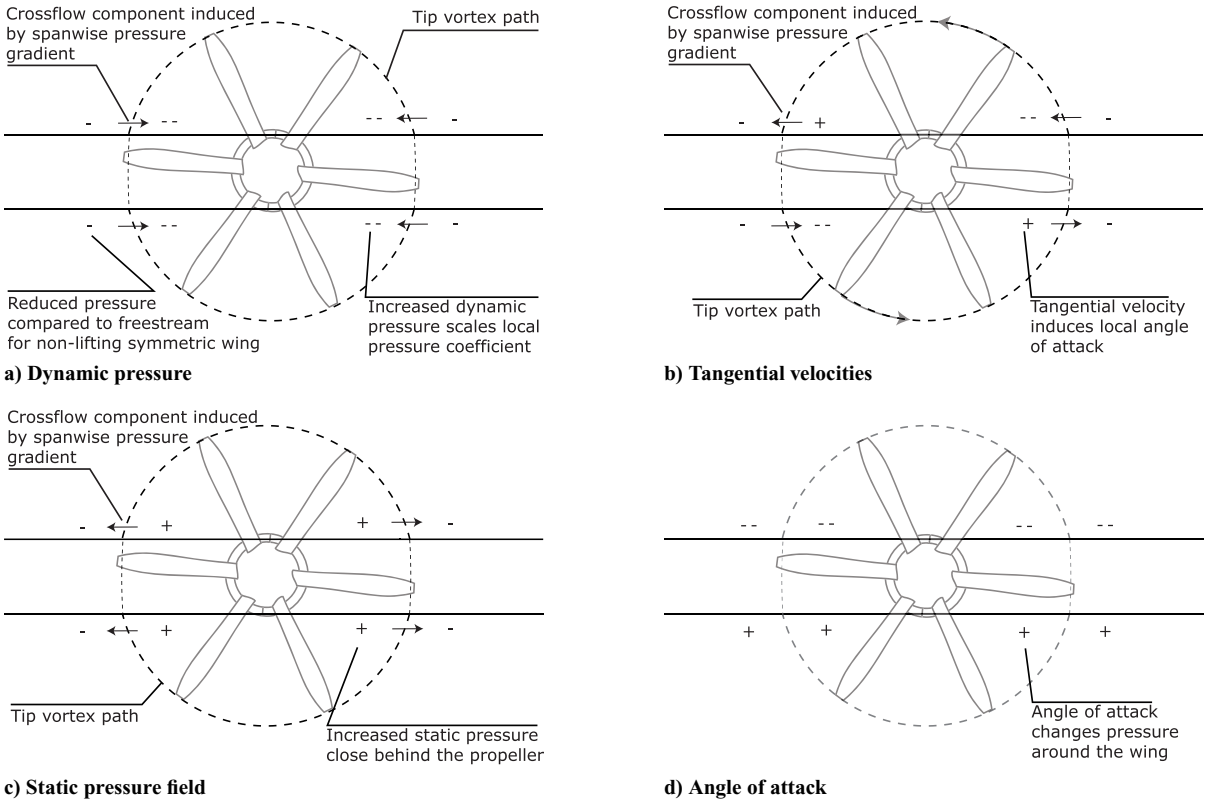

a) Dynamic pressure

b) Tangential velocities

c) Static pressure field

d) Angle of attack

Fig. 2 Schematic illustration of the four main contributions to the spanwise pressure gradients induced by propeller–wing interaction on a lifting wing. Front view.

thus completely change for a lifting wing, a scenario that is not included in Felli's work. Additionally, the setup by Felli [7] consists of a separated propeller and wing, while the integration of the nacelle with the wing has a significant impact on the flow development [3,8]. Finally, the driving mechanisms may vary between low-lift and high-lift conditions, as viscous effects become more dominant. Nonetheless, the described mechanisms suggest that the characteristics of the helical vortex system of the slipstream are driving the deformation of the slipstream.

The primary focus of this study is therefore to investigate how the characteristics of the slipstream, such as the ratio between azimuthal[§] and longitudinal vorticity, and vorticity concentration, affect the resulting slipstream deformation. By manipulating thrust and torque coefficients of the propeller, which are directly related to the amount of vorticity shed into the slipstream and therefore the structure of the helical vortex system, we analyze changes to the slipstream deformation and whether this agrees with existing theory on the deformation mechanisms. Thrust and torque coefficients are controlled by variations in blade pitch, advance ratio, and the number of blades in an experimental wind tunnel campaign. Measurements include seven-hole pressure probe measurements of various cross-sections of the slipstream around the wing, as well as oil flow visualizations and infrared (IR) thermography to track the slipstream trajectory on the wing surface. The findings of this paper add to the understanding of the propeller–wing(–flap) aerodynamic interaction, specifically from a flow dynamics perspective. This is essential to the development of closely coupled propeller–wing designs and optimization of next-generation propeller-driven aircraft.

A. Dataset and Related Work

As experimental data on propeller–wing–flap configurations is particularly scarce in literature, the full dataset is made available for future study in [9]. It is expected to be particularly valuable for numerical validation, as the slipstream deformation can be used as an excellent test of the aerodynamic fidelity in simulations, an approach also used by Ribeiro et al. [10].

Furthermore, the same model geometry has been used in various previous publications across various topics. The experiments

[§]In the direction of rotation.

described in this paper are a direct extension of those described by the authors in [8]. Comparisons of wake measurements of the distributed propeller configurations versus the single propeller configuration are presented in [11]. Barker et al. [12] investigate the aeroacoustic interactions of the wing with a single propeller using uRANS. Monteiro et al. [13] perform experimental measurements of the aeroacoustical interactions in a distributed propeller configuration, while Yang et al. [14] investigate the same configuration numerically using a hybrid large-eddy simulation and Ffowcs-Williams and Hawkings method.

II. Methods

A. Model Geometry

The model used in the experiments is a straight wing with a chord length of 0.3 m and a span of 1.25 m. It has a single slotted flap of $0.3c$, which can be deployed to discrete positions using six brackets that mount it to the main wing element. The wing model features an NLF-mod22(B) airfoil, designed and tested by Boermans and Rutten [15]. A single nacelle was fitted to the centerline of the model, which houses an electric motor to drive the propeller. The nacelle is mounted at a downward angle of 5 deg with respect to the wing chord with the flap nested. Figure 3 shows a schematic drawing of the model. The wing model geometry is available from the Zenodo repository [16].

The wing model was fitted with the TUD-XPROP-S propeller, a six-bladed propeller with straight blades and a diameter of 203.2 mm.

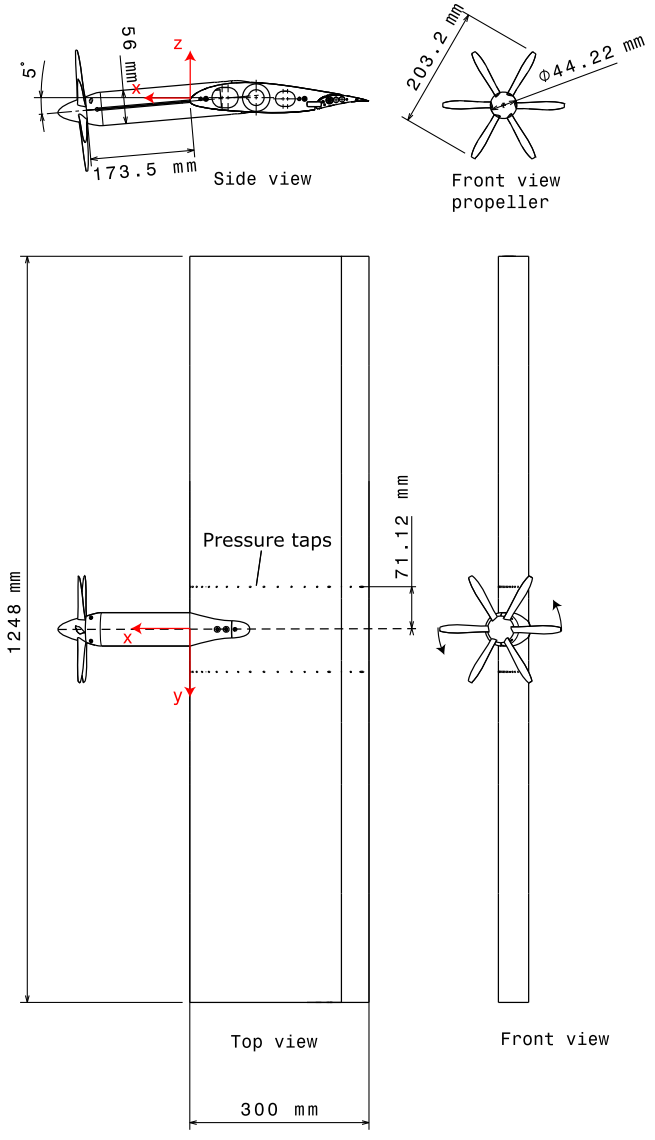

Fig. 3 Technical drawing of the wind tunnel model.

In this experiment, a three-bladed version of the propeller was also used, which is otherwise identical to the regular configuration. The performance of the (six-bladed) TUD-XPROP-S has been detailed by de Vries et al. [17], and its geometry is available on the Zenodo repository [18].

B. Experimental Setup

Experiments were performed at the Low Turbulence Tunnel (LTT) of the Delft University of Technology, a closed-section tunnel with a test section 2.6 m in length. Its octagonal cross-section measures 1.8 m wide by 1.25 m high. The test section is slightly divergent to mitigate buoyancy effects. In a cross-section at the center of the (empty) test section, the variation of dynamic pressure is less than $\pm 0.05\%$ [19]. All measurements were taken at a free-stream velocity of $V_\infty = 30$ m/s, at which the average turbulence intensity is 0.02% [20]. The wing model was mounted vertically in the wind tunnel test section, spanning the entire height of the wind tunnel. This results in solid blockage of less than 0.2%, based on the airfoil thickness-to-chord ratio of $(t/c) = 0.17$ and $\lambda_{2D} \approx 3$ (from the graphs by Barlow et al. [21]). As we did not measure the total drag coefficient of the wing, the wake blockage cannot be calculated. However, based on the original measurements of the NLFmod22(B) profile by Boermans and Rutten [15], it is expected to be less than 0.1% for all tested configurations. Slipstream blockage at the maximum tested thrust coefficient is less than 0.3%. The measurement data presented in this paper are all uncorrected. No mitigation of junction flows was applied, as previous experiments of the same setup have shown the effects of junction flows on the propeller region to be negligible [8].

For this paper, the flap is either in its nested configuration or deployed to a deflection of $\delta_f = 15$ deg, with an overlap of $dx = 0.08c$ and a gap of $ds = 0.05c$. Figure 4 shows the definitions of deflection δ_f, gap ds, and overlap dx. The latter represents a typical takeoff condition and matches one of the flap deflection settings of previous studies with the same wing model [8,10]. During all measurements, a black vinyl layer was applied to the wing, which will be addressed in the section on thermography setup. The nacelle and outer wing sections, as well as a strip of 1 cm around the pressure taps, were not covered. On the main element upper surface, a zigzag strip was placed at $x/c = 0.1c$ to mitigate low-Reynolds-number effects such as laminar separation bubbles and improve comparison with numerical simulations. Other surfaces (i.e., the main element's lower surface and both sides of the flap) were left to transition naturally. This was done to match previous experiments with the same model [8]. The experimental setup is visualized in Figs. 5 and 6, including some aspects of the measurement techniques that were applied. Further details of the setup for each measurement technique are given further ahead in this paper.

We applied various measurement techniques to measure the development and deformation of the slipstream, both on the wing surface and in the flow. Several measurement planes perpendicular to the freestream capture the state of the slipstream at various chordwise positions on the wing. These measurement planes, taken with a seven-hole pressure probe, provide total and static pressure measurements, as well as all three velocity components of the flow. The seven-hole data were supplemented with oil flow visualization of both the upper and lower wing surfaces, as well as IR thermography on both wing sides.

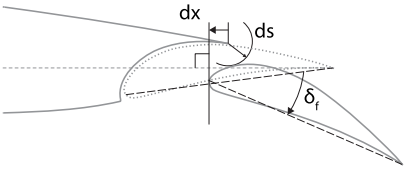

Fig. 4 Definition of the flap deflection δ_f, gap ds, and overlap dx.

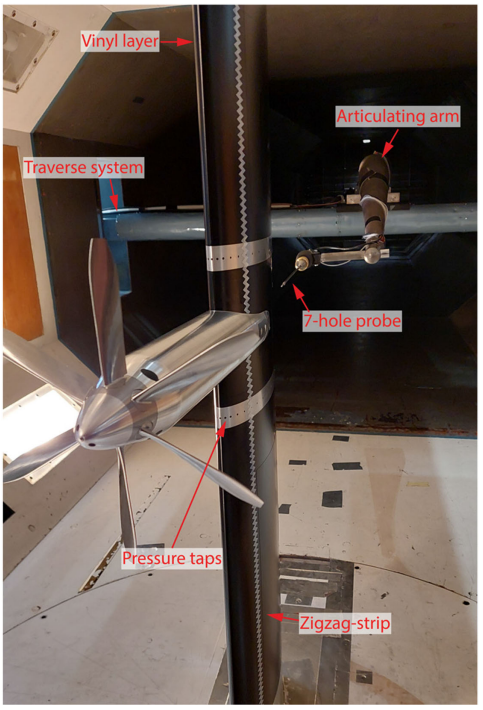

Fig. 5 Overview of the wing model in the tunnel with the downstream probe traverse system.

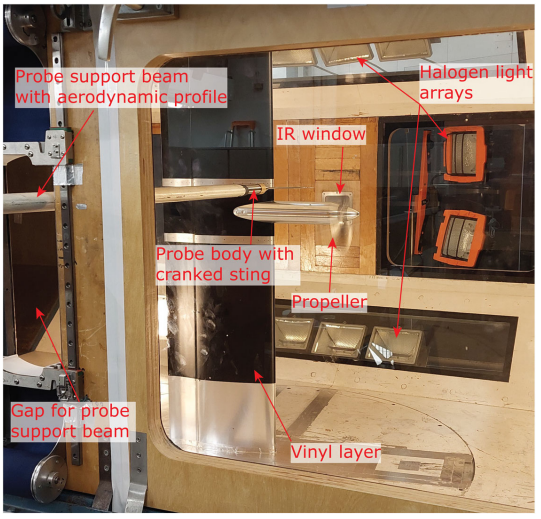

Fig. 6 Overview of the experimental setup with the cranked probe and thermography setup.

1. *Seven-Hole Pressure Probe Setup*

Pressure probe measurements were taken with a Surrey Sensors Ltd. USM-ID7HP-050224-3.0 Digital 7-hole Pressure Probe. It contains an internal differential pressure sensor that outputs data at a maximum rate of 1 kHz. It was used with two custom probe stings, one straight (Fig. 7a) and one with a 90 deg crank (Fig. 7b), both with a tip diameter of 2 mm. The straight probe was used for measurements on the wing's upper surface and behind the wing. A three-axis traversing system was positioned downstream of the test section in the diffuser of the wind tunnel, with an articulated arm reaching upstream into the test section on which the probe was mounted. The probe sting was aligned with the test section's central axis, and the tip could reach from just behind the wing (in all configurations) up to around $x/c = 0.03$,[¶] depending on the angle of attack of the wing. Figure 8 shows an illustration of the setup of the straight probe system. The cranked probe was used to reach behind the propeller and the lower surface of the wing. It was mounted on an aerodynamic profile that entered the test section from the side, using a traverse system aligned with the test section side. This system could only move perpendicular to the freestream direction when measuring but could be repositioned along the test section between measurements without losing its alignment to the wind tunnel. The cranked probe setup is illustrated in Fig. 9.

We took pressure measurements of planes perpendicular to the freestream direction at various chordwise stations over the wing, as well as along spanwise lines just above the wing surface, as illustrated in Fig. 10a. We scanned the measurement planes by moving the probe through the planes in straight lines at a traverse speed of 7.5 mm/s, while measuring continuously at a data rate of 250 Hz. Exceptions are the measurements with the three-bladed propeller, which were taken at a traverse speed of 15 mm/s to reduce measurement time and mitigate overheating of the electric motor that drives the propeller. The traverse paths for the measurement planes are illustrated in Fig. 10 for $\alpha = 8$ deg and $\delta_f = 15$ deg. Note that these paths will vary slightly for each configuration, as the planes are always perpendicular to the freestream direction, not the wing chord, and hence are dependent on the wing model angle of attack and flap deflection. The streamwise coordinates of the propeller, nacelle, and cove planes are equal in all tested configurations, while their vertical coordinates are adjusted for the orientation of the model. The *METE* plane is adjusted for the location of the main element trailing edge (METE), while the wake plane is vertically centered on the flap trailing edge and positioned 5 cm downstream of it. The traverse paths were manually adjusted to minimize the traverse distance (and therefore measurement time) while capturing the entire slipstream as it deforms and displaces over the wing.

In postprocessing, the measurement data are passed through a Savitzky–Golay filter [22] to reduce noise of the pressure sensor while maintaining the sampling resolution. From the seven-hole pressure measurements, we calculate the local total and static pressure measurements, as well as all three components of velocity. For these calculations, we use the methodology of Shaw-Ward et al. [23]. The required calibration of the pressure probes was performed by the manufacturer for each of the probe stings separately. The calibrations were performed after the experiment, matching the orientation of the probe body during the experiments using the internal accelerometer.[**]

The measurement planes were chosen to visualize different stages of the deformation. The propeller plane gives the initial condition of the slipstream and is mainly used as a check for the selected theoretical operating conditions (see Sec. III.A). The plane behind the nacelle blend captures the initial deformation of the slipstream from the interaction with the wing leading edge. Together with the planes at the main element trailing edge and the flap trailing edge plane, the entire deformation over the wing upper surface is visualized. Similarly, the cove plane and flap trailing edge plane show the deformation on the lower surface of the wing. Additionally, the cove plane yields the inflow condition of the flap when it is deflected. The planes on the upper surface of the wing and the flap trailing edge plane are all measured using the straight probe setup. The propeller and cove planes were captured using the cranked probe setup.

In all cases, a minimum normal distance between the probe center and wing surface of 4 mm was maintained. We verified that this was the minimum distance required to avoid significant channel flow occurring between the probe tip and the wing surface. This was tested by placing the probe directly normal to one of the pressure taps on the wing and moving it closer until the pressure tap reading deviated from the initial value by more than 5%.

The surface planes aligned with the wing upper surface consist of a primary plane at 4 mm from the surface and a secondary surface at 11 mm from the wing surface. The secondary plane was chosen based

[¶]In wind tunnel frame, with the origin at the wing quarter-chord.

[**]During the experiment itself, the stings were aligned to the wind tunnel axes by laser. Data from the probe accelerometer was then recorded and reported to the manufacturer for subsequent calibration. The manufacturer aligned the probes by laser and checked the orientation via the accelerometer values.

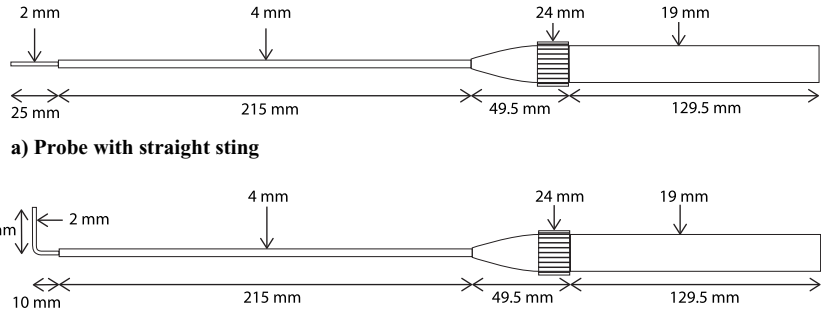

Fig. 7 Technical drawing of the seven-hole pressure probe with each custom sting.

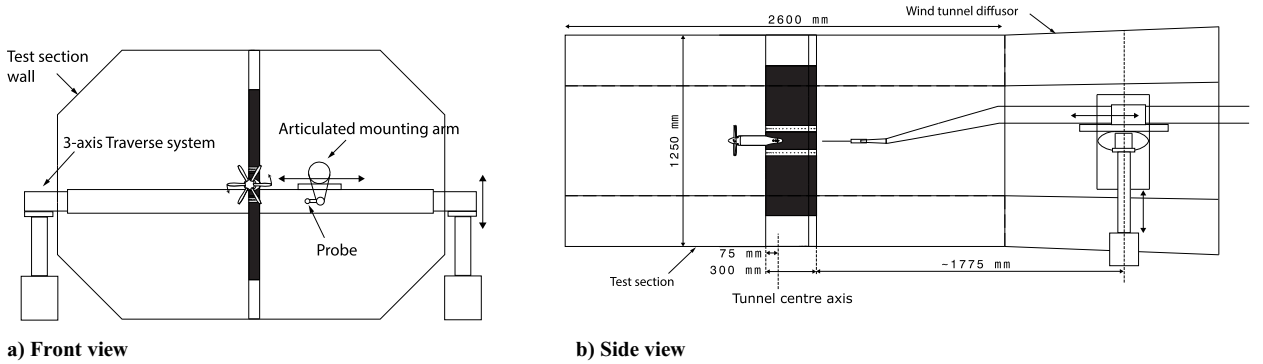

Fig. 8 Illustration of the traverse setup for the straight probe. Dimensions in mm.

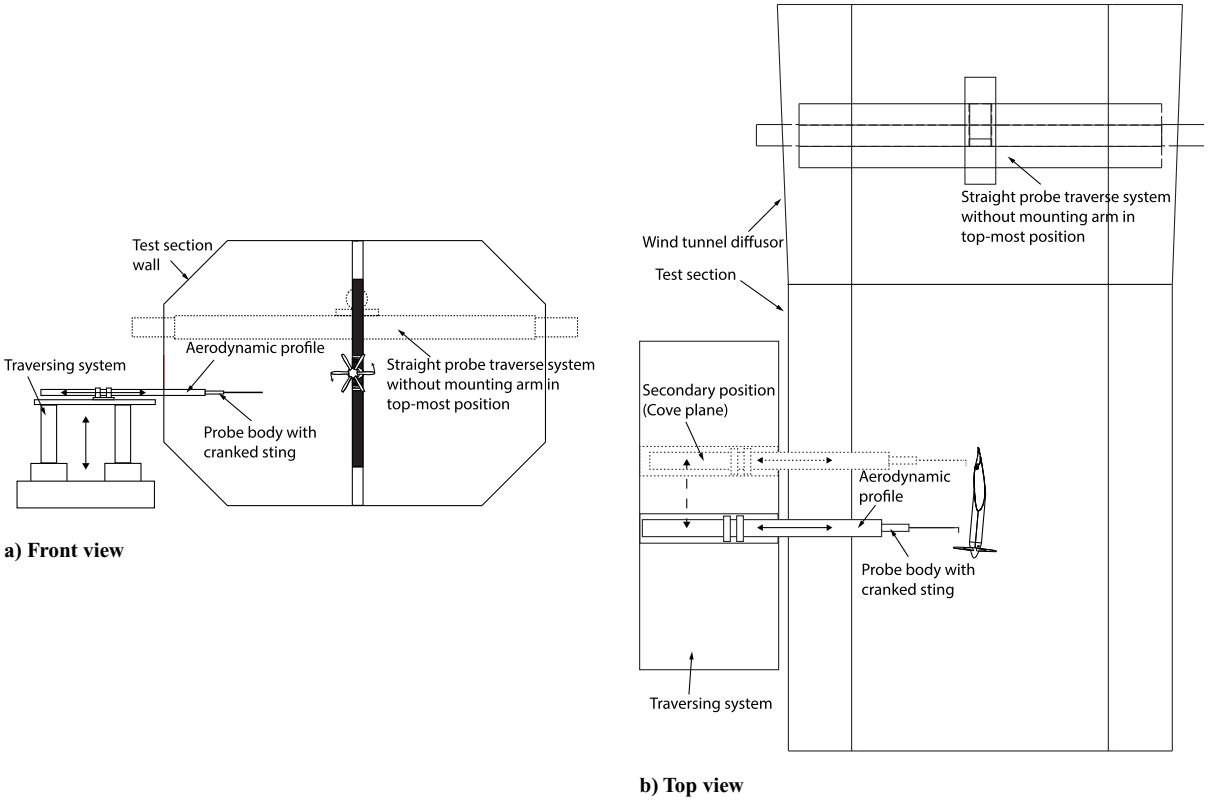

Fig. 9 Illustration of the traverse setup for the cranked probe.

on numerical simulations (from Ribeiro et al. [10]) to be outside the boundary layer, since the calibration of the pressure probe to calculate the velocity vector can become unreliable if it operates within a strong pressure gradient over the width of the probe tip. This secondary plane therefore only covers a portion of the main element near the trailing edge, where the boundary layer is thickest (see Fig. 10a). The surface planes are composed of spanwise continuous lines (see Fig. 10g). The (discrete) chordwise positions of these lines are chosen

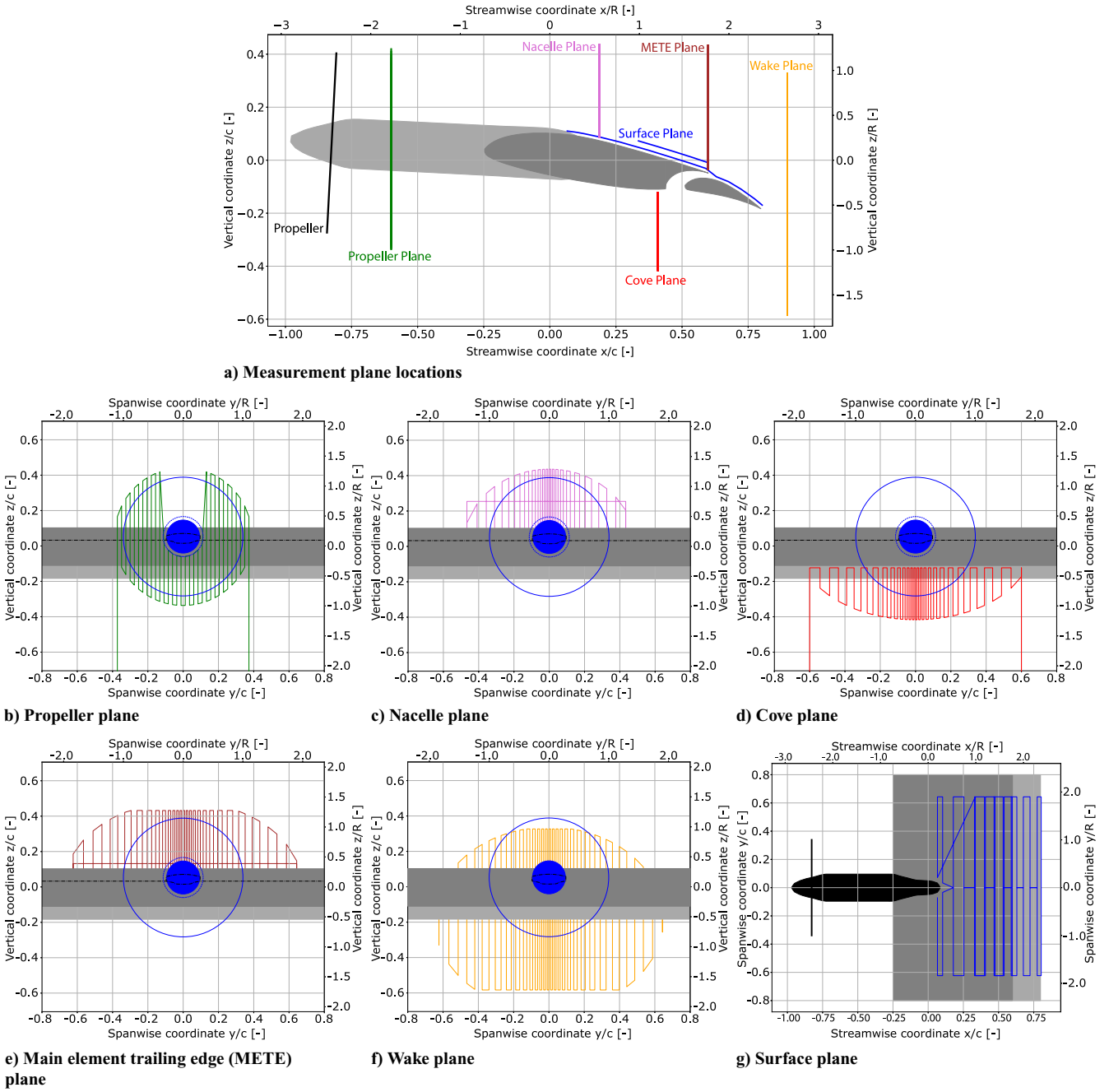

Fig. 10 Illustration of the locations and corresponding paths of the measurement planes at $\alpha = 0$ deg, $\delta_f = 0$ deg. View in freestream direction, perpendicular to the measurement planes.

to be aligned with the chordwise locations of the pressure taps of the wing (the locations of which are specified in [8]), complemented with the most forward location reachable by the mounting arm and the main element and flap element trailing edges.

2. *Oil Flow Setup*

We visualized the wing surface flow on both sides of the wing using oil flow visualization. The oil was a mixture of paraffin oils (i.e., 80% Shell Ondina 15 and 20% Shell Ondina 32) with 20 drops of A-680 fluorescent oil additive added per 30 mL of oil. The oil was illuminated using Philips TL-D BLB Blacklight Fluorescent Tube lights in combination with a 400W UV spotlight. Images were captured with the wind tunnel turned on, using cameras (Sony Alpha 7-II and Nikon D7500) mounted on tripods on both sides of the test section. Each camera was equipped with a 470 nm low-pass filter, which filters most of the light from the fluorescent tube lights and their reflections but passes the wavelength of the fluorescent oil additive. During all oil flow visualizations, the traverse system for the probe was present in the wind tunnel, positioned at the top of the tunnel. The articulated mounting arm was removed, however. Figure 11 illustrates the oil flow setup. Oil flow visualization images were post-processed using Adobe Lightroom (version 7.4.1). Image contrast was maximized, and images were edited for highlights and shadows to improve the visibility of oil flow paths. All images were subsequently denoised and sharpened using the AI-assisted tools provided by Lightroom.

3. *Thermography Setup*

We utilized IR thermography to measure the change in skin friction coefficient on the wing surface resulting from the additional velocities in the slipstream. Numerical simulations [10] had shown that c_f was

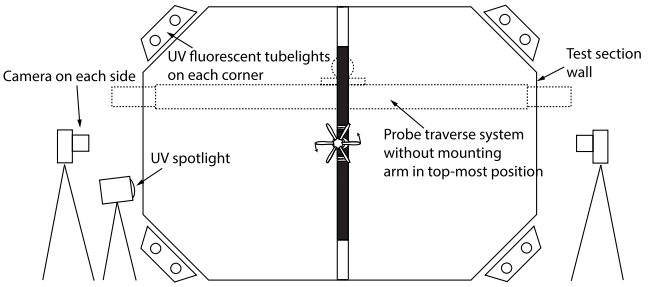

Fig. 11 Experimental setup for the oil flow visualizations.

an effective parameter to determine the area of the wing that is washed by the slipstream, and thereby the displacement of the slipstream edge as it moves over the wing. Measuring this displacement on the wing surface based on total pressure or velocity gradients is generally difficult due to the viscous losses in the boundary layer.

IR thermography is typically used for detection of flow separation and boundary-layer transition fronts (see, for instance, Zuccher and Saric [24] and Simon et al. [25]). It relies on the convective heat transfer $\dot{q} = h(T_W - T_\infty)$, with heat transfer coefficient $h = (1/2)c_f V_\infty (k_f/\nu)$, where T_W is the wall temperature, T_∞ is the fluid temperature, c_f is the skin friction coefficient, V_∞ is the freestream velocity, k_f is the thermal conductivity of the fluid, and ν is the kinematic viscosity. By keeping $\dot{q}$ constant, for instance, by heating the surface of the model externally by electric heating, the wall temperature T_W will change with the local skin friction coefficient c_f. This is captured by measuring the emitted IR radiation using IR cameras.

The experimental setup for the thermography measurements consisted of two Optris PI 640 IR cameras, mounted on each side of the wind tunnel behind special IR bandpass windows. The cameras were covered with boxes lined with aluminum tape to shield them from external IR sources. Since the wind tunnel model is made from aluminum, which has a high heat capacity and thus dissipates local changes in temperature, a black vinyl foil with an average thickness of 100 μm was placed on the wing. This allows a temperature contrast to be achieved in the thermography measurements. To achieve the necessary temperature difference between the wing surface and the fluid flow, the model was heated externally using arrays of halogen lights. Halogen lamps fitted with IR bulbs were placed on the diagonals of the test section, with additional regular halogen lights placed around the test section sides. Figure 12 summarizes the experimental setup of thermography measurements.

The workflow for thermography was as follows. The halogen lights were turned on during pressure probe measurements and left on until thermal equilibrium was reached on the wind tunnel model, monitored using the IR cameras. Once probe measurements were completed and thermal equilibrium was reached, the cameras were reset and thermography images were captured for various advance ratios in quick succession. This means that the probe traverse mechanism, including the articulating arm, was present in the wind tunnel during all of the thermography measurements. The probe was always centered in the wind tunnel, behind the model, when thermography measurements were taken. The various advance ratios include the design values for the experiment for each wing configuration, as well as an advance ratio near zero thrust. The latter served as a reference condition for the wing, minimizing the effect of the slipstream on the wing surface flow, resulting in a skin friction coefficient representative of the unblown wing. Each measurement consisted of 100 consecutive images captured by the cameras. In postprocessing, these images are averaged to reduce noise. Subsequently, we subtracted the reference measurement of near-zero thrust from the measurement at design values. This yields a measurement of where the skin temperature changes significantly due to an increase in skin friction on the wing caused by the slipstream.

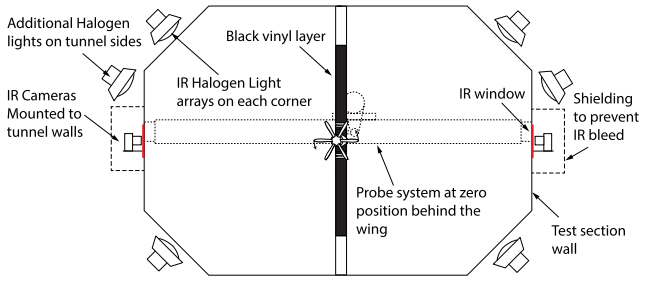

Fig. 12 Experimental setup for the IR thermography.

4. *On the Efficacy of IR Thermography*

Our initial purpose to capture the change in c_f caused by the propeller blowing on the upper surface (which was already tripped by the zigzag strip), rather than boundary-layer transition, was met with mixed success. Based on numerical results by Ribeiro et al. [10], the change in c_f between the unblown and blown parts of the wing surface was expected to be around a factor of 5. This is significantly lower than the typical change in c_f due to boundary-layer transition, which is around a factor of 10 [25]. It was therefore unknown ahead of time whether the setup we used would result in enough contrast to visualize the slipstream path. In practice, we found that we were able to capture the change in c_f, but at a very low contrast. The measured change in temperature due to propeller blowing was close to the minimum temperature sensitivity of the cameras, resulting in a poor signal-to-noise ratio.

On the lower surface of the wing, however, we achieved much more consistent visualizations of the slipstream path. This opposed expectation, since the change in c_f due to propeller blowing on the pressure side is much lower than on the suction side. The more consistent results can be attributed to the thermography actually visualizing the boundary-layer transition. Unlike the suction side, the pressure side of the wing was not tripped, and the boundary layer likely remained laminar up to the cove of the main element in most configurations, since the airfoil was originally designed for natural laminar flow [15]. The turbulence in the slipstream, however, trips the wing boundary layer, resulting in a clear change in skin friction compared to the unblown parts of the wing.

Although the IR thermography did not fully work as originally intended, the authors believe that there is potential in using IR thermography to visualize the slipstream deformation on the wing surface. This goes for both the method of measuring the slipstream-induced boundary-layer transition of the wing and the method of directly measuring the change in c_f due to the increased velocities in the propeller slipstream. We mainly include the description of the thermography in this paper as a reference for readers who want to apply a similar technique. Results may be improved by improving the surface preparation, for instance, by using conductive paint to increase the achievable contrast. Additional (internal) surface heating and more sensitive cameras would also improve the setup.

In the results of this paper, the thermography measurements are only used to support interpretation of the oil flow images. This combination leads to improved interpretation of the slipstream path on the wing surfaces. Figure 13 shows an example of how we combined these results to determine the slipstream paths. The correct overlap of oil flow images and thermography measurements was performed manually, using the nacelle and wing and flap trailing edges as reference.

C. Choice of Operating Conditions

The main objective of this experiment is to determine the dependency of slipstream deformation on the slipstream helix angle. Additionally, we investigate the impact of tip vortex strength for a given slipstream helix structure. We can decompose the helical vortex system of the slipstream into longitudinally and azimuthally oriented vorticity, as is common in slipstream tube models (e.g., [26]), in which case the helix angle depends on the ratio between the longitudinal and azimuthal parts. This decomposition is illustrated in Fig. 14. The tip vortex strength changes if the same total vorticity

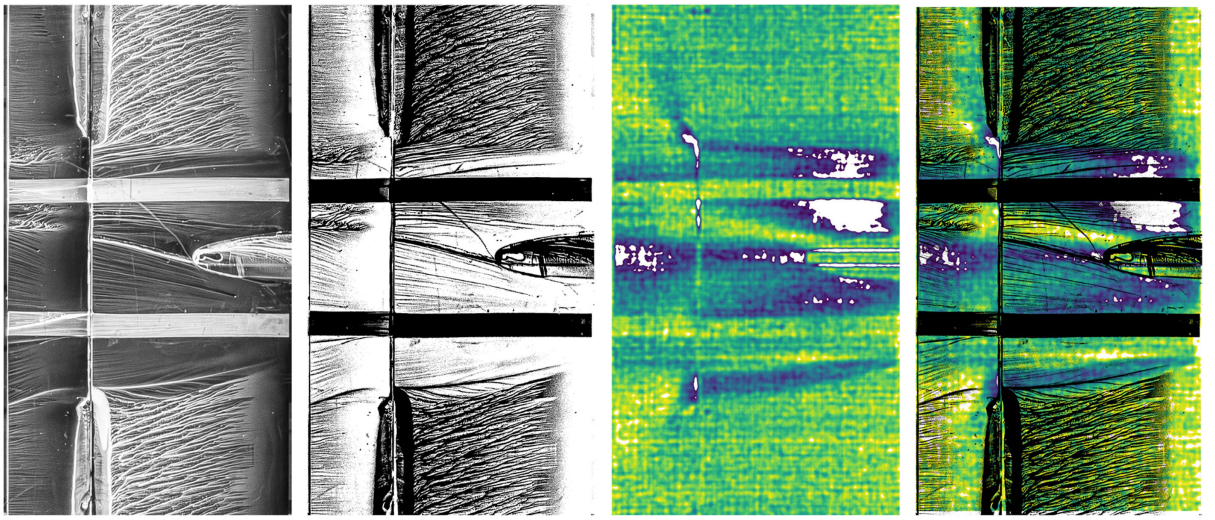

a) Processed oil flow image b) Extracted oil traces c) Thermography measurement d) Overlay of traces and thermography

Fig. 13 Example of processing steps to combine oil flow and thermography results. Wing lower surface view, freestream from right to left.

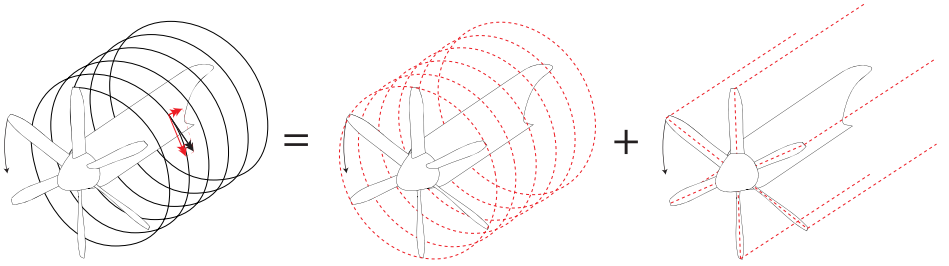

Fig. 14 Decomposition of the helical vortex system of the slipstream into azimuthally and longitudinally oriented vorticity.

in the slipstream is achieved with fewer blades or if the helix angle remains the same but the total vorticity in the slipstream is reduced. In practice, the only control we have to vary these quantities for a given propeller is by varying the advance ratio, blade pitch, and number of blades. In this paper, we assume that longitudinal vorticity in the slipstream scales directly with the torque coefficient $Q_c = (Q/\rho V^2 D^3)$, while azimuthal vorticity scales with thrust coefficient $T_c = (T/\rho V^2 D^2)$. We can then discretely vary either Q_c or T_c by selecting the appropriate combination of blade pitch angle $\beta_{0.7R}$ and advance ratio J. Changing the number of blades while maintaining equal Q_c and T_c should then lead to a direct change in the strength of each individual tip vortex but equal total vorticity in the slipstream.

Unfortunately, not enough experimental data are available to determine these configurations. We therefore simulated propeller performance for various blade pitch settings and numbers of blades across a wide range of advance ratios using a blade element momentum (BEM) model. Installed on the wing, the propeller operates in a nonuniform inflow field resulting from the circulation on the wing. To verify this will not change the operating conditions of the propeller to an extent that will invalidate the BEM simulations, we applied the method by van Arnhem [27] to predict the propeller performance at an inflow angle. These simulations were run at an inflow angle of 5 deg, as this is the highest angle that the method was validated at. The results are summarized in Fig. 15. It shows calculated $Q_c - T_c$ curves for the six-bladed (solid) and three-bladed (dashed) propellers at specific blade pitches. Black curves represent the performance in isolated conditions, while the red curves signify the curves for the propeller with an inflow angle of 5 deg.

The curves in Fig. 15 show very little difference between the isolated and installed performance. We attribute this to the limited advance ratios that are achievable in the experimental setup due to torque limitations of the electric motors. At lower advance ratios, the calculated curves deviate more between isolated and installed conditions, but within the range achievable in the experiment, there is little difference. It should be noted that the apparent angle of incidence for the propeller during the experiment is likely to exceed 5 deg, particularly in high-lift configuration. However, based on Fig. 15, they are unlikely to shift to such a degree that

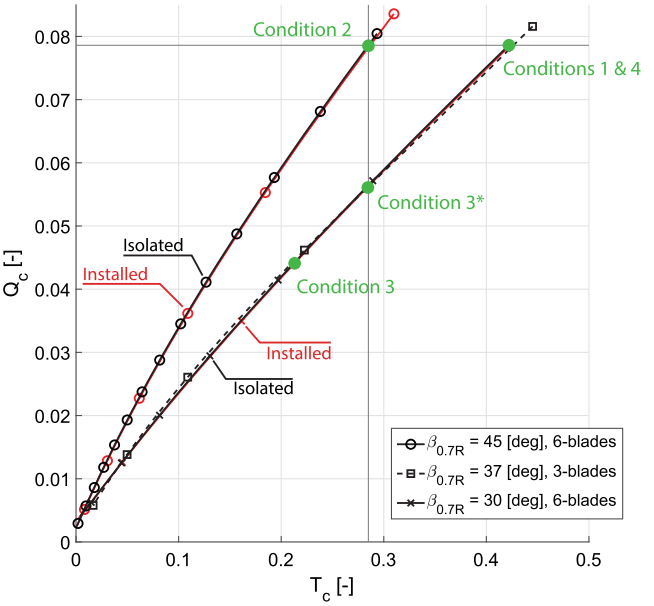

Fig. 15 Calculated performance curves for the TUD-XPROP-S with six and three blades, in isolated and installed conditions. Chosen operating conditions marked in green.

Table 1 Summary of numerical predictions of propeller performance for operating conditions used in the experiment (configurations will be referred to by their handle)

Condition	Handle	N_b	$\beta_{0.7R}$, deg	J	T_c	Q_c
1	High-T_c/high-Q_c	6	30	0.800	0.422	0.079
2	Low-T_c/high-Q_c	6	45	1.195	0.284	0.079
3* (target)	— —	6	30	0.904	0.284	0.056
3 (actual)	Low-T_c/low-Q_c	6	30	0.984	0.210	0.044
4	Three-bladed	3	37	0.717	0.284	0.079

they invalidate the main objective of the selected operating conditions, which is focused on primarily changing T_c and Q_c one factor at a time.

The performance curves from Fig. 15 can then be used to select specific operating conditions that allow us to discretely vary T_c and Q_c. The selected conditions are summarized in Table 1. We chose the six-bladed propeller with $\beta_{0.7R} = 30$ deg at $J = 0.8$ as our baseline condition, as it matches a previous experiment with the same model [8]. This condition represents the maximum Q_c that can be achieved by the electric motors used in the experiment. At the same Q_c, the same propeller with $\beta_{0.7R} = 45$ deg produces significantly lower T_c, leading to our second condition. We then find the condition for the propeller with $\beta_{0.7R} = 30$ deg that matches this lower T_c to arrive at the third condition. Finally, we add the three-bladed propeller with $\beta_{0.7R} = 37$ deg at $J = 0.717$, which is predicted to produce the same T_c and Q_c as the first condition. This enables us to compare the effect of the same total vorticity concentrated in fewer, stronger tip vortices. Unfortunately, due to an oversight, the third condition was performed at $J = 0.984$, rather than $J = 0.904$, during the experiment. This means the thrust coefficients do not match exactly between conditions 2 and 3.

Measurements of each of the conditions summarized in Table 1 (except condition 3*) were taken for three wing configurations: $\alpha = 0$ deg with $\delta_f = 0$ deg, $\alpha = 8$ deg with $\delta_f = 0$ deg, and $\alpha = 8$ deg with $\delta_f = 15$ deg. This allows for the analysis of the dependencies of slipstream deformation on slipstream characteristics for low and high lift conditions, as well as flap deflection.

III. Results and Discussion

In this section, we compare the measurements for each of the propeller conditions. We first analyze the measurements in the propeller plane to verify the propellers operated sufficiently close to design conditions. This is followed by a discussion of the impact of thrust and torque coefficients on the slipstream deformation for the wing in low-lift configuration ($\alpha = 0$ deg, flap nested) and high-lift configuration ($\alpha = 8$ deg, $\delta_f = 15$ deg). We define the slipstream deformation as the redistribution of total pressure and vorticity in the slipstream in a shape that deviates from the circular shape of the propeller disk.

Additional measurements at $\alpha = 8$ deg and flap nested are available in the attached dataset [9]. These measurements are not discussed further in this paper. For both the low-lift and the high-lift configurations, we will show changes to the slipstream deformation due to the propeller condition from two perspectives: the volumetric flow (based on the probe measurement planes) and the wing surface flow (based on the oil flow visualization and thermography measurements).

A. Thrust and Torque Coefficient Verification

Since the design points are determined from numerical simulation, it is worth verifying that the propeller is operating roughly at the desired condition. To this end, we analyze the measurements of the total pressure coefficient $C_{p,t} = ((p_t - p_{s,\infty})/q_\infty)$ in the propeller plane (Fig. 10b). Figure 16 shows the distributions of $C_{p,t}$ in that plane for the various conditions. The missing parts of the distribution were obscured by the nacelle during the experiment and could therefore not be measured. Since the propeller increases the total pressure of the flow, the slipstream can be defined by $C_{p,t} > 1$. Note the step-like artifacts at the outer border of the slipstream. These are artifacts of interpolation caused by the limited resolution in the spanwise direction and the very strong gradient in total pressure at the slipstream edge. This gradient is nearly discontinuous and could not be accurately fitted with typical interpolation methods.[††]

As expected, it shows that the case for $\beta_{0.7R} = 30$ deg at $J = 0.8$ gives the highest total pressure coefficients, as it produces the most thrust. The three-bladed configuration ($\beta_{0.7R} = 37$ deg at $J = 0.717$) was designed to produce the same thrust coefficient; however, the distribution (Fig. 16d) shows much lower values of $C_{p,t}$ and a very different distribution. Particularly at the edge of the slipstream, much less total pressure is added to the flow. This indicates that the tips of the three-bladed propellers were separated during operation.

We can integrate the distributions of Fig. 16 to calculate an equivalent thrust coefficient $T_C^* = \int((C_{p,t} - 1)/2D^2)\,\mathrm{d}A$, given for each condition in Table 2. As a part of the distribution is missing, this value cannot be compared to the design thrust coefficient T_c. Nonetheless, it gives an indication of the relative difference in loading between the different propeller conditions and whether this aligns with the design aim of each condition.

In a similar fashion, we compare the different conditions in terms of swirl in the slipstream to determine whether they operate at comparable torque coefficients. We compare the various cases based on the tangential velocity component induced at $\psi = 270$ deg$(y/R = 0)$. At this location, the y-component of the velocity vector is exclusively dependent on the local torque and not affected by the wing upwash component. The radial distributions of the y-component of velocity are shown in Fig. 17. It shows that condition 1 ($\beta_{0.7R} = 30$ deg, $J = 0.8$) and condition 2 ($\beta_{0.7R} = 45$ deg, $J = 1.195$) yield very similar tangential velocity distributions. Additionally, condition 4 ($\beta_{0.7R} = 37$ deg, $J = 0.717$, $N_b = 3$) induces tangential velocity of comparable order of magnitude and distribution, despite the separation of the blade tips. Assuming the distributions of Fig. 17 as representative for the entire disk, we can calculate an equivalent torque coefficient $Q_c^* = \iint(u\Delta v r^2/V_\infty^2 D^2)\,\mathrm{d}r\,\mathrm{d}\psi$ [28]. The equivalent torque and thrust coefficients are reported in Table 2.

From Table 2 it is clear that conditions 1 and 2 indeed operate at comparable Q_c, but different T_c. Conditions 3 and 4 do not satisfy their original design points, as condition 3 was operated at the wrong advance ratio and condition 4 suffered blade tip separation that was not predicted. We therefore do not have a direct comparison where only Q_c is varied at constant T_c. However, condition 3 happens to operate at a T_c/Q_c ratio that is near to condition 1, meaning that the slipstream helix angle is comparable but with a lower total vorticity. Furthermore, the change in Q_c between conditions 2 and 3 is still much larger than the change in T_c. This still allows for the analysis of the relative dominance of T_c and Q_c for the slipstream deformation. In fact, in the remainder of this section we will show that the thrust coefficient has very little impact on the slipstream deformation, meaning that we can still use condition 3 to show the impact of the torque coefficient. Additionally, while condition 4 suffers from separation on the blade tips, it still operates at a Q_c close to condition 1, meaning that it can offer an additional comparison for the comparable torque cases.

B. Assessment of Slipstream Deformation in Low-Lift Configuration

As a result of the propeller–wing aerodynamic interaction, the propeller slipstream deforms from its initial, circular shape. In the low-lift condition, this deformation mostly occurs in the form of a shearing effect of the two halves of the slipstream that pass the wing on each side of the wing and spanwise elongation near the wing surface. This is shown for each of the propeller conditions in Fig. 18 by means of the distributions of $C_{p,t}$ in the wake plane. Dashed lines show propeller tip and root, and wing leading edge (MELE) and flap trailing edge (FLTE). The effect of the tested propeller conditions on

[††]The results in this paper have all been generated in Python with *matplotlib.pyplot.tricontourf*.

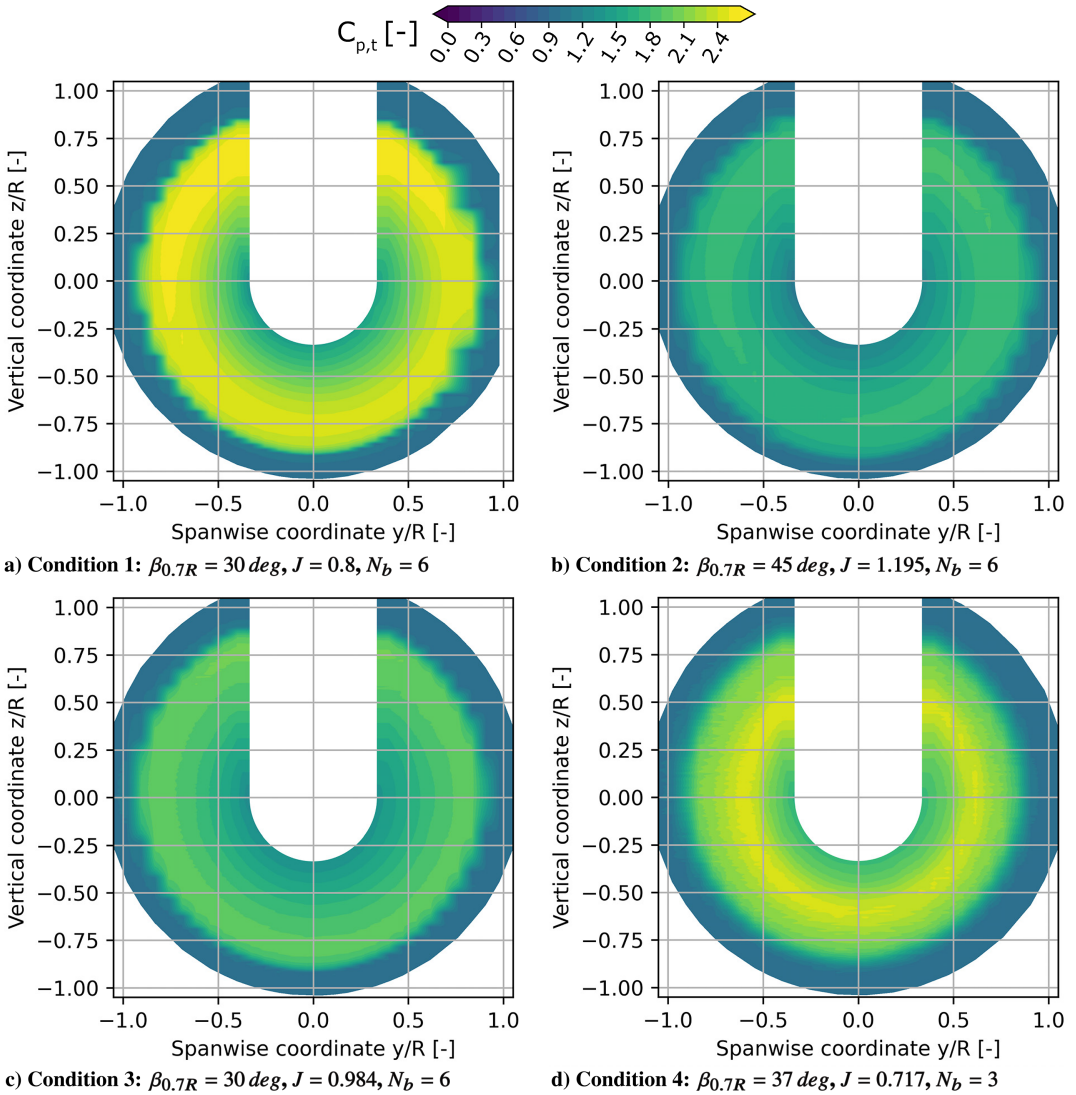

a) Condition 1: $\beta_{0.7R} = 30\,deg$, $J = 0.8$, $N_b = 6$

b) Condition 2: $\beta_{0.7R} = 45\,deg$, $J = 1.195$, $N_b = 6$

c) Condition 3: $\beta_{0.7R} = 30\,deg$, $J = 0.984$, $N_b = 6$

d) Condition 4: $\beta_{0.7R} = 37\,deg$, $J = 0.717$, $N_b = 3$

Fig. 16 Distributions of total pressure coefficient $C_{p,t}$ in the plane behind the propeller. Missing area was obscured by the nacelle.

Table 2 Equivalent thrust and torque coefficients, allowing for comparison of propeller performance

Condition	N_b	$\beta_{0.7R}$, deg	J	T_c^*	Q_c^*	T_c^*/Q_c^*
1	6	30	0.800	0.2747	0.0724	3.79
2	6	45	1.195	0.1781	0.0664	3.00
3	6	30	0.984	0.1428	0.0402	3.55
4	3	37	0.717	0.2320	0.0749	3.10

the slipstream deformation is relatively limited in low-lift conditions. Figure 18 shows that comparable torque coefficients (Figs. 18a and 18b) result in nearly identical deformation, while varying both torque and thrust coefficients (Fig. 18c) results in a clear reduction of the deformation. For the latter condition, the slipstream remains closer to its initial, circular shape, with less elongation of the upper-left and lower-right regions of the slipstream and less inboard movement of the lower-left and upper-right regions. The three-bladed propeller condition (Fig. 18d) shows comparable deformation of the slipstream to Figs. 18a and 18b, with the major difference that the gradient of the total pressure coefficient at the edge of the slipstream is much more gradual due to the blade tip separation.

The difference in deformation is visualized more clearly in Fig. 19, which compares the slipstream shape of the high-T_c/high-Q_c condition with the other conditions by use of the contour line for $C_{p,t} = 1.05$. As the slipstream can be identified by the addition of total pressure in the flow, this contour yields the outer

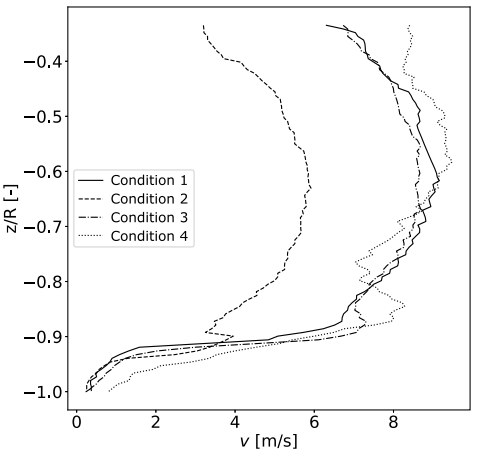

Fig. 17 Radial distribution of the y-component of velocity at $\psi = 270$ deg.

boundary and therefore shape of the slipstream. Note that we take $C_{p,t} = 1.05$ instead of $C_{p,t} = 1.00$ to mitigate effects of noise and uncertainty on the pressure measurements and achieve a clear image of the outer border of the slipstream. Since the gradient at this border is very strong, $C_{p,t} = 1.05$ is still an accurate representation of the slipstream edge.

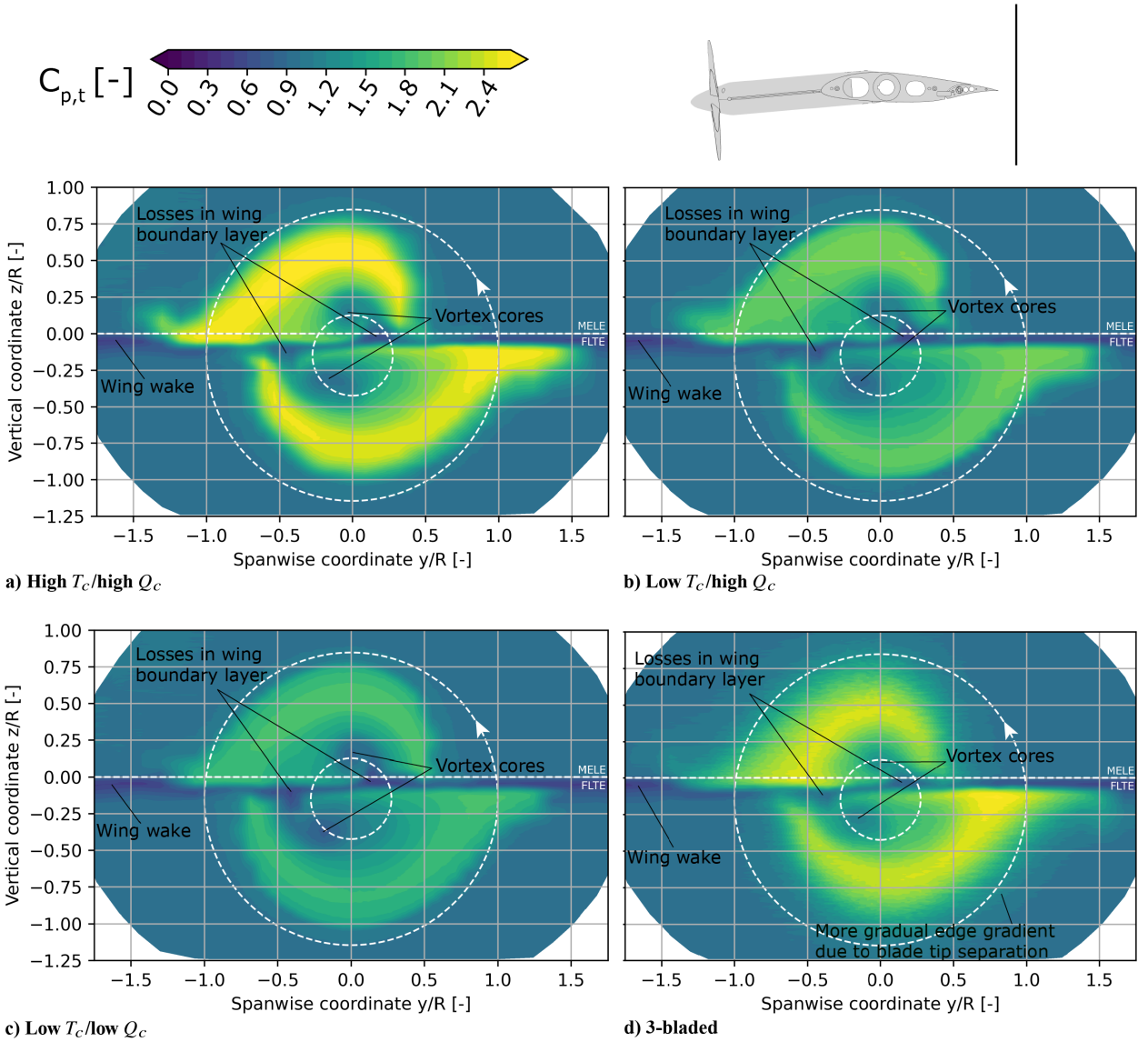

Fig. 18 Distributions of $C_{p,t}$ behind the flap TE, visualizing the total slipstream deformation. $\alpha = 0$ deg, $\delta_f = 0$ deg.

Figure 19a shows that the low-T_c/high-Q_c condition has slightly larger regions of pressure loss near the wing surface, while the low-T_c/low-Q_c condition (Fig. 19b) particularly has larger pressure loss areas near the slipstream center. The former will be discussed in more detail in the treatment of the high-lift configuration later in this paper. The latter are associated with vortices, as seen from the in-plane velocity vectors shown in Fig. 20. Since the low-T_c/low-Q_c condition adds significantly less total pressure coefficient to the slipstream, pressure losses in the viscous cores of these vortices show up more clearly on the contour line of Fig. 19b.

As the viscous losses in the wing boundary layer reduce the total pressure coefficient, it is difficult to determine the exact area of the wing that is washed by the slipstream (hereinafter referred to as the *washed area*) from the total pressure measurements alone. Figures 21 and 22 therefore visualize the surface flow (upper and lower surfaces, respectively) using the oil flow visualization images. It shows the extracted oil flow highlights, overlapping the high-T_c/high-Q_c condition (in black) with high-T_c/low-Q_c (blue), low-T_c/low-Q_c (red), and the three-bladed propeller (green). It should be noted that the shearlines visualized by the oil flow are not direct streamlines and are affected by many factors such as gravity and oil thickness. Slight changes in the oil lines are therefore not always directly analogous to changes in flow condition and require careful interpretation.

Similar to the overall slipstream deformation, the surface flow is nearly identical for comparable Q_c. Figure 21a shows a small spanwise shift in the flow structure on the upper surface trailing edge. For low-T_c/low-Q_c, the oil flow lines near the slipstream edge clearly show less spanwise convection compared to the baseline (see Figs. 21b and 22b). The difference is largest at the locations where the blade moves toward the wing surface (i.e., the upgoing blade side on the lower surface and the downgoing blade side on the upper surface). Additionally, the region behind the nacelle in Fig. 22b shows less spanwise shift for the low-T_c/low-Q_c condition, indicating a smaller crossflow component. The three-bladed case surface flow patterns are nearly identical to the six-bladed baseline, with some deviations at the outer boundaries of the slipstream. Again, this can be attributed to the outer edge of the slipstream being diffused due to the separation at the blade tips. The significant shift in the separation bubble in Fig. 22c is best explained by the turbulence around the slipstream edge resulting from the blade tip separation, as the shear lines in the oil flow otherwise indicate no significant shift in slipstream edge trajectory. For all conditions, however, the exact slipstream edge is difficult to identify, and on the upgoing blade side of the upper surface, no clear flow structures can be compared.

The crossflow behind the nacelle in Fig. 22c seems to be slightly different, which we also attribute to the blade tip separation. The total pressure distributions of Fig. 16d revealed the loading to be more toward the blade root. This could result in a slight difference in

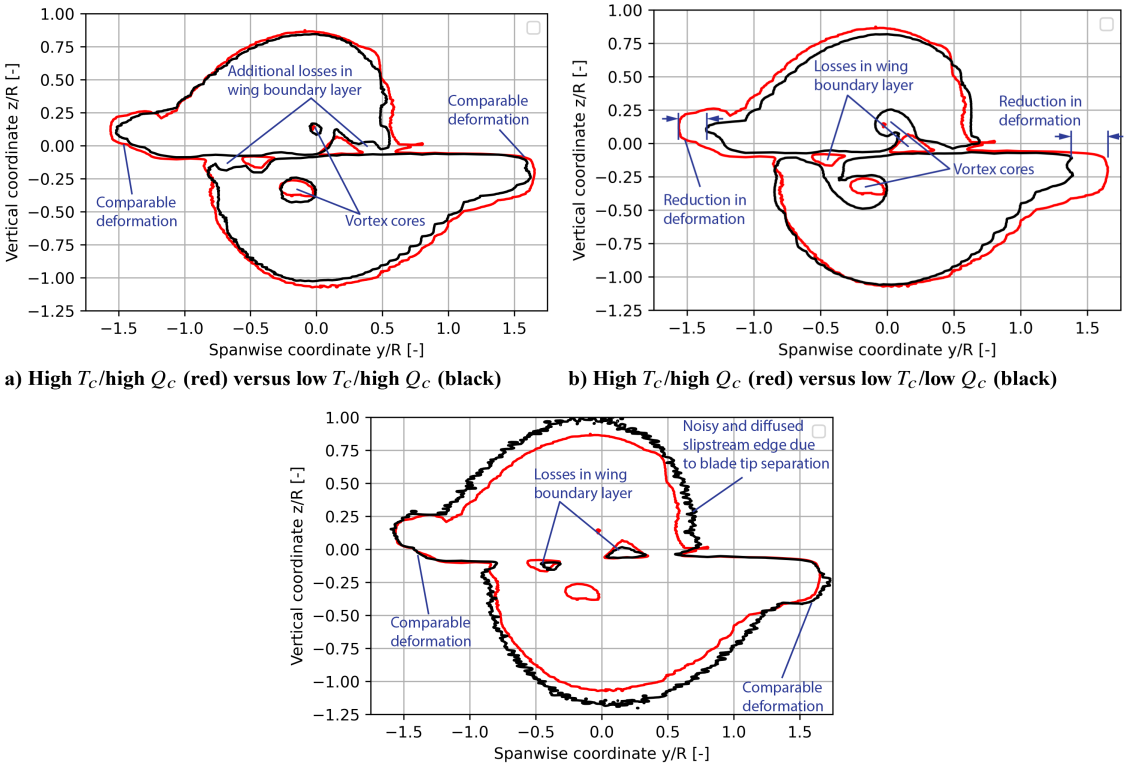

a) High T_c/high Q_c (red) versus low T_c/high Q_c (black)

b) High T_c/high Q_c (red) versus low T_c/low Q_c (black)

c) Six-bladed (red) versus three-bladed (black)

Fig. 19 Contour lines of $C_{p,t} = 1.05$ behind the flap TE, comparing the deformation of each condition with the high-T_c/high-Q_c baseline. $\alpha = 0$ deg, $\delta_f = 0$ deg.

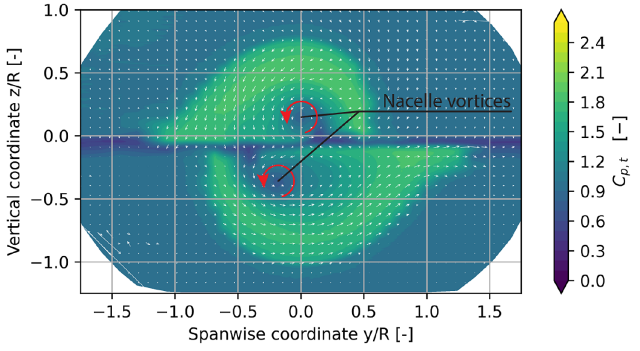

Fig. 20 Vector plot of the in-plane velocities, overlaid on the distribution of $C_{p,t}$. Low-T_c/low-Q_c condition, $\alpha = 0$ deg, $\delta_f = 0$ deg.

vorticity rolling into the nacelle vortex, which would then change the crossflow on the wing surface. The differences with the high-T_c/high-Q_c condition are relatively small, however, and not in the order of magnitude of the low-T_c/low-Q_c condition.

In an attempt to clearly identify the slipstream edge and quantify the change in deformation, we used both the thermography measurements and the oil flow image extracts to determine the edges of the washed area for the various conditions. The results are shown in Fig. 23a for the upper surface and Fig. 23b for the lower surface. Figure 13 in Sec. II shows how these images are constructed. Note that the slipstream edge in Fig. 23b is only traced up to the main element cove area, as it was not possible to accurately estimate the position of the slipstream edge beyond that. Furthermore, the three-bladed propeller condition is not included, since the blade tip separation diffuses the slipstream edge and can have an unexpected

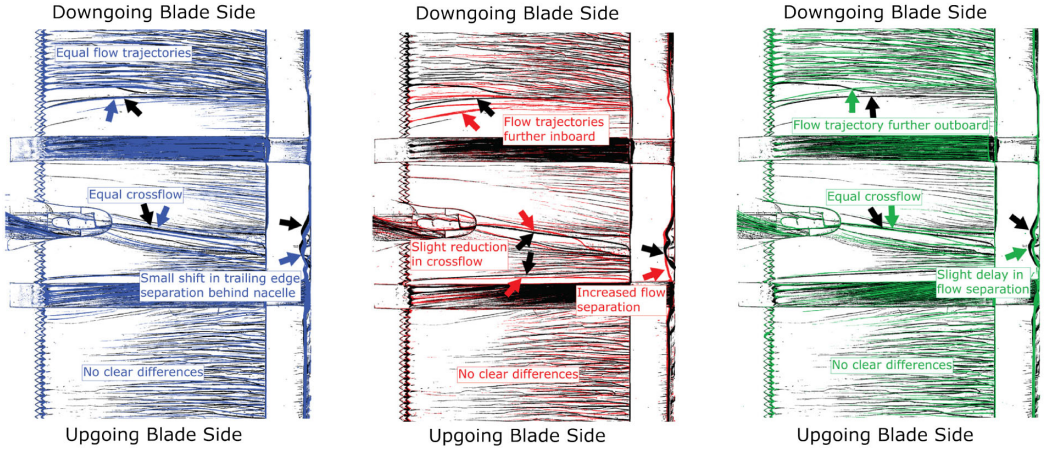

a) High T_c/high Q_c (black) versus low T_c/high Q_c (blue)

b) High T_c/high Q_c (black) versus low T_c/low Q_c (red)

c) High T_c/high Q_c (black) versus three-bladed (green) propeller

Fig. 21 Overlays of (zoomed in) processed oil flow images, comparing high-T_c/high-Q_c with each of the other conditions. Upper surface, $\alpha = 0$ deg, $\delta_f = 0$ deg. Freestream from left to right.

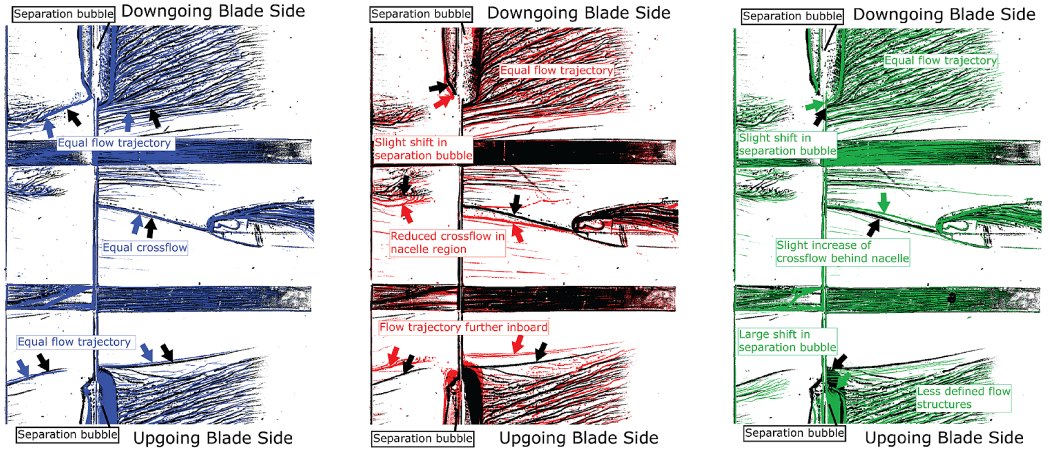

a) High T_c/high Q_c (black) versus low T_c/high Q_c (blue)

b) High T_c/high Q_c (black) versus low T_c/low Q_c (red)

c) High T_c/high Q_c (black) versus three-bladed (green) propeller

Fig. 22 Overlays of (zoomed in) processed oil flow images, comparing high-T_c/high-Q_c with each of the other conditions. Lower surface, $\alpha = 0$ deg, $\delta_f = 0$ deg. Freestream from right to left.

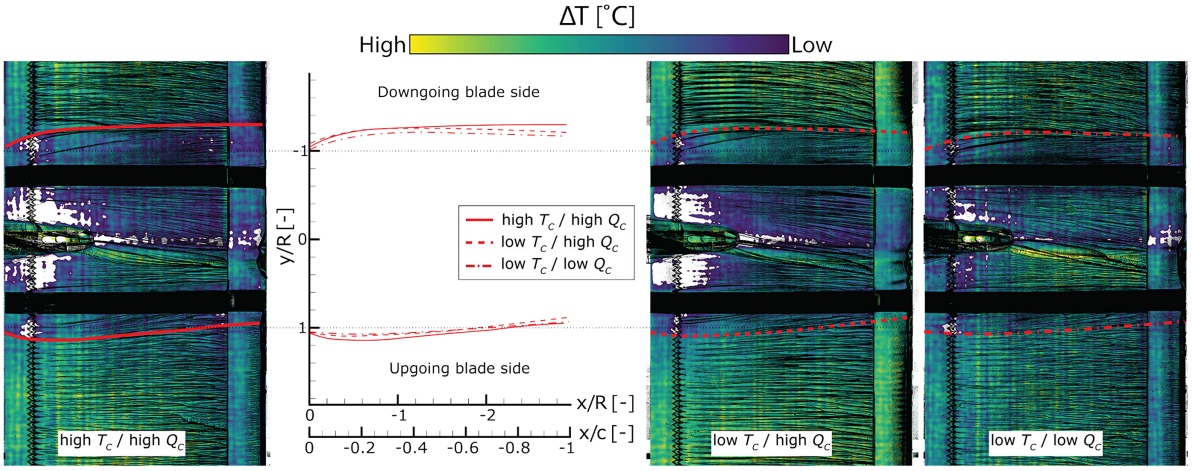

a) Upper surface. Freestream from left to right

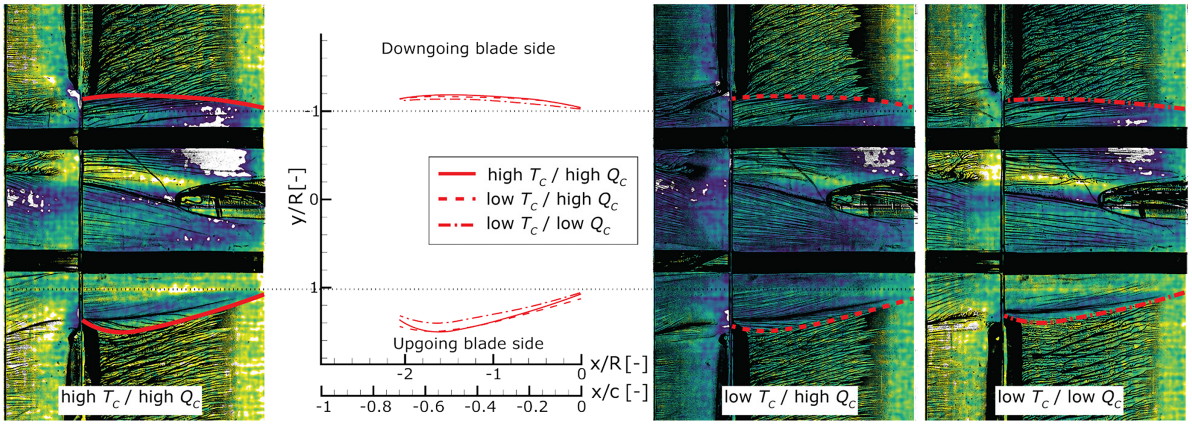

b) Lower surface. Freestream from right to left

Fig. 23 Comparisons of slipstream edge paths over the wing, estimated from thermography and oil flow visualization. $\alpha = 0$ deg, $\delta_f = 0$ deg.

impact on the transition of the wing boundary layer, on which the thermography is strongly dependent.

Figure 23 clearly visualizes that the change in deformation is largest on the upper surface downgoing blade side and the lower surface upgoing blade side. The maximum difference in spanwise displacement between the high-T_c/high-Q_c case and the low-T_c/low-Q_c case is $0.1R$ on the lower surface upgoing blade side, which is roughly 20% of the total displacement of the high-T_c/high-Q_c case. On the upper surface downgoing blade side, the difference between the high-T_c/high-Q_c and the low-T_c/low-Q_c is again around $0.1R$, roughly 40% of the total displacement for the high-T_c/high-Q_c case at that edge. The change in displacement is thus equivalent in both cases but is significantly more impactful on the upper surface. It should be noted that these values are extracted from qualitative measurements and are therefore subject to some uncertainty, but they do show a coherent trend where the washed area of the wing is significantly affected by the propeller condition.

Between T_c and Q_c, the torque coefficient is dominant for the slipstream deformation, where a lower torque coefficient results in less spanwise displacement of the slipstream edge on the wing surface and less redistribution of the total pressure in the slipstream from its initial, circular shape. In Fig. 23, the conditions with comparable Q_c show nearly the same trajectory of the slipstream edge regardless of T_c setting. From the mechanisms proposed by Felli [7] (see Figs. 1 and 2 in Sec. I), it could be expected that a significant change in T_c would particularly affect the leading-edge deformation, as the azimuthal vorticity will directly impact the vortex imaging effect. Figure 23 only shows small changes at the wing leading edge for the different loading conditions, however. This may be explained by the change in spanwise pressure gradients at the leading edge, imposed by the change in thrust coefficient, opposing the vortex imaging effects. Unfortunately, we cannot definitively draw this conclusion, as the current experiment does not yield enough data in this region, and the quantification of the slipstream path has some uncertainty. Although the thermography does visualize the slipstream path near the leading edge fairly well (particularly on the upper surface), it is insufficient to investigate the relative contributions of the vortex image and spanwise pressure gradient effects to the total deformation. Time-accurate (or phase-accurate) measurements or simulations that resolve the tip vortices near the leading edge will prove crucial in further investigating the relative balance between these effects.

C. Assessment of Slipstream Deformation in High-Lift Configuration

In the high-lift configuration, the impact of the propeller condition on the slipstream deformation is much more significant than in the low-lift configuration. Figure 24 shows the distribution of the total pressure coefficient just behind the flap trailing edge for the various propeller conditions, while Fig. 25 again visualizes the slipstream shape by means of the $C_{p,t} = 1.05$ contour lines. Overall, the conditions with comparable Q_c (Figs. 24a and 24b) again show comparable deformation (visualized well in Fig. 25a), but with a clear deviation on the upgoing blade side of the upper slipstream part. There is an apparent gap in the slipstream of the low-T_c/high-Q_c condition (Fig. 25a), which also occurs in the low-T_c/low-Q_c condition (Fig. 25b). Figures 24b and 24c show regions of low-total pressure coefficient here. These are secondary vortex structures, as illustrated by the in-plane velocity vectors for the low-T_c/low-Q_c condition in Fig. 26. Furthermore, the low-T_c/low-Q_c condition has significantly more pressure losses inside the slipstream, as is evident from Fig. 25b. These phenomena will be discussed further at a later stage in this section.

Beyond the differences in the distribution of total pressure for the internal parts of the slipstream, the differences in slipstream deformation follow the same patterns as in the low-lift conditions. The low-T_c/high-Q_c condition (Fig. 25a) is largely comparable to the baseline, while the low-T_c/low-Q_c condition (Fig. 25b) has significantly less deformation on both the upgoing and downgoing blade sides. The low-T_c/high-Q_c condition does show a

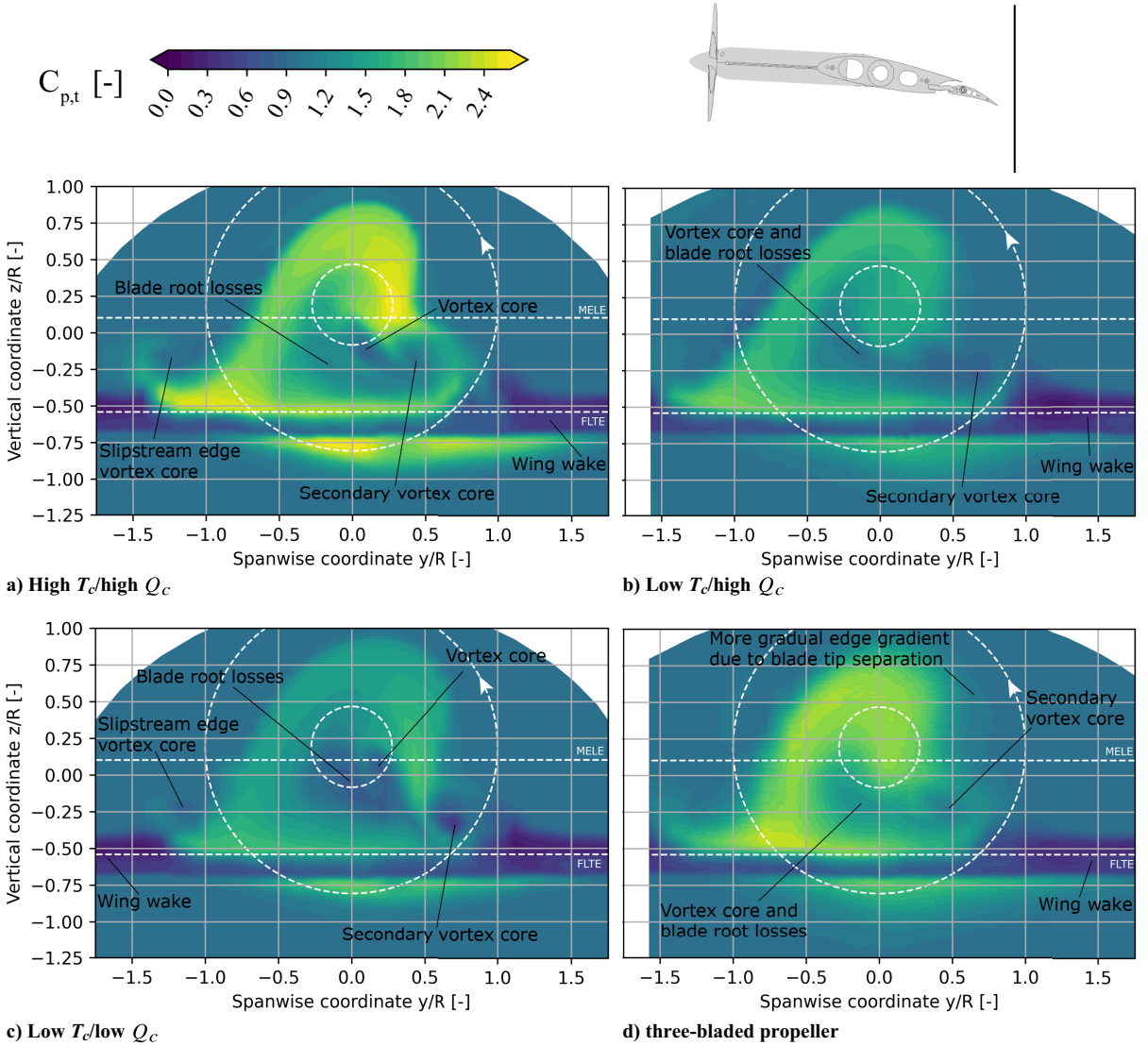

Fig. 24 Distributions of $C_{p,t}$ behind the flap TE, visualizing the total slipstream deformation. $\alpha = 8$ deg, $\delta_f = 15$ deg.

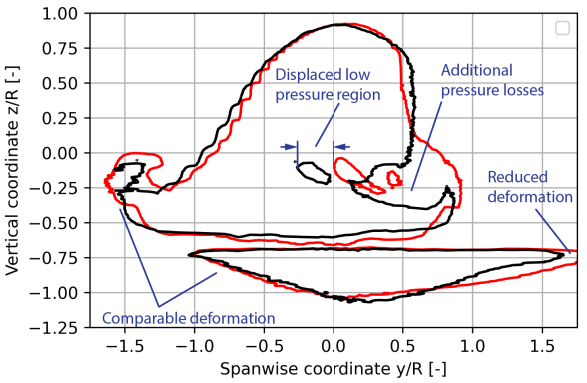

a) High T_c/high Q_c (red) versus low T_c/high Q_c (black)

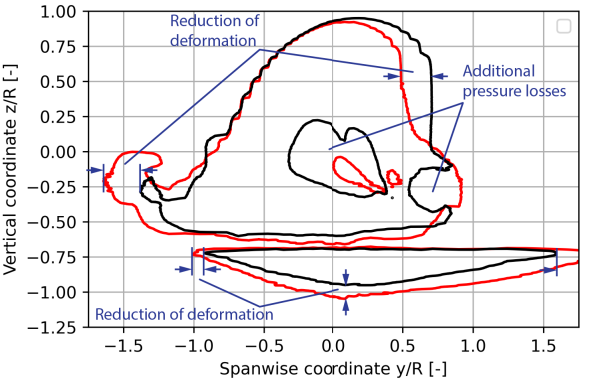

b) High T_c/high Q_c (red) versus low T_c/high Q_c (black)

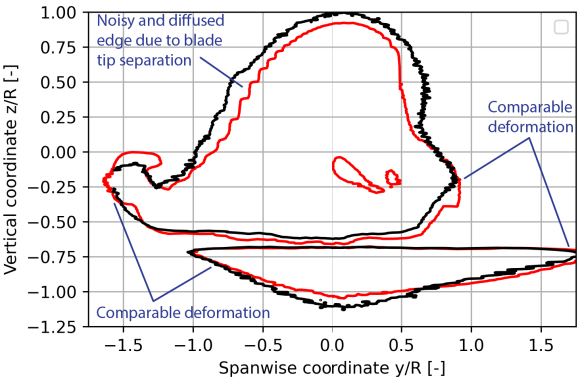

c) Six-bladed (red) versus three-bladed (black)

Fig. 25 Contour lines of $C_{p,t} = 1.05$ behind the flap TE, comparing the deformation of each condition with the high-T_c/high-Q_c baseline. $\alpha = 8$ deg, $\delta_f = 15$ deg.

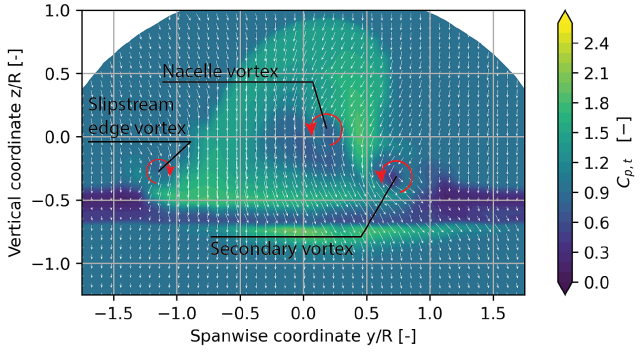

Fig. 26 Vector plot of the in-plane velocities, overlaid on the distribution of $C_{p,t}$. Low-T_c/low-Q_c condition, $\alpha = 8$ deg, $\delta_f = 15$ deg.

reduction in slipstream deformation on the upgoing blade side of the lower part of the slipstream (see Fig. 25a). From the measurements, it is not entirely clear whether this is a reduction in slipstream deformation or just a result of dissipation of the total pressure at the slipstream edge. The oil flow visualizations (discussed below) do not show a clear deviation in slipstream deformation, however. The three-bladed propeller condition (Fig. 25c), finally, shows comparable deformation compared to the high-T_c/high-Q_c baseline, but with a more diffuse boundary. A region of lower total pressure seems to be present here, like for the low-T_c/high-Q_c and low-T_c/low-Q_c conditions, but it does not show in the contour line of Fig. 25c. This can likely be attributed to the diffuse slipstream boundary resulting from the separation on the blade tips.

In general, the comparisons of shear lines extracted from the oil flow visualizations (Figs. 27 and 28) show similar results to the low-lift configuration, although with much more emphasized deviations. The low-T_c/high-Q_c condition is nearly identical to the baseline on the upper surface (Fig. 27a), with small deviations developing toward the aft section of the main element on the downgoing blade side. These deviations can also be seen in the contour line comparison of Fig. 25a, which reveals these deviations to be only local. The flow trajectories on the upgoing blade side of the lower surface (Fig. 28a) show a more significant change in deformation, which we are unable to explain based on current data. Apart from the extension on the lower surface upgoing blade side, however, the slipstream shape is still highly comparable to the high-T_c/high-Q_c condition. The low-T_c/low-Q_c condition (Fig. 27b) shows less outboard displacement at the edges and less crossflow behind the nacelle. The three-bladed condition (Fig. 27c) again yields nearly identical flow trajectories on the upper surface, with more diffuse outer boundaries and some small differences in crossflow trajectories behind the nacelle.

On the lower surface, all conditions show nearly identical flow trajectories behind the nacelle. The trajectories are almost fully aligned in the chordwise direction, indicating little to no crossflow. In the high-lift configuration, very little of the slipstream passes the lower surface, as the freestream and wing upwash convect most of the slipstream over the upper surface. As a result, the nacelle-root vortex on the lower surface is very weak, and there is little locally induced crossflow. This is strongly dependent on the configuration and particularly prominent for the wing model used in this experiment, due to the relatively large distance between the propeller and wing leading edge.

As with the low-lift configuration, quantifying the slipstream edge trajectory from the oil flow images alone is difficult and prone to error. Figure 29 therefore shows the overlays of thermography and oil flow highlights to improve the estimation of the slipstream edge.[‡‡] The majority of the change in deformation again occurs on

[‡‡]Note that for the upper surface at low-T_c/high-Q_c condition, only the oil flow image is shown, as there was no thermography measurement available.

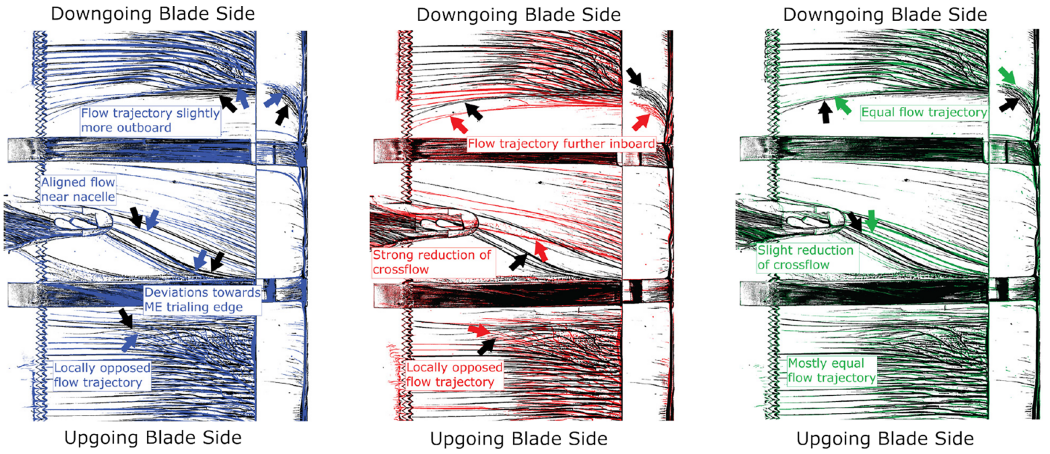

a) High T_c/high Q_c (black) versus low T_c/high Q_c (blue) **b) High T_c/high Q_c (black) versus low T_c/low Q_c (red)** **c) High T_c/high Q_c (black) versus three-bladed propeller (green)**

Fig. 27 Overlays of (zoomed in) processed oil flow images, comparing high-T_c/high-Q_c with each of the other conditions. Upper surface, $\alpha = 8$ deg, $\delta_f = 15$ deg. Freestream from left to right.

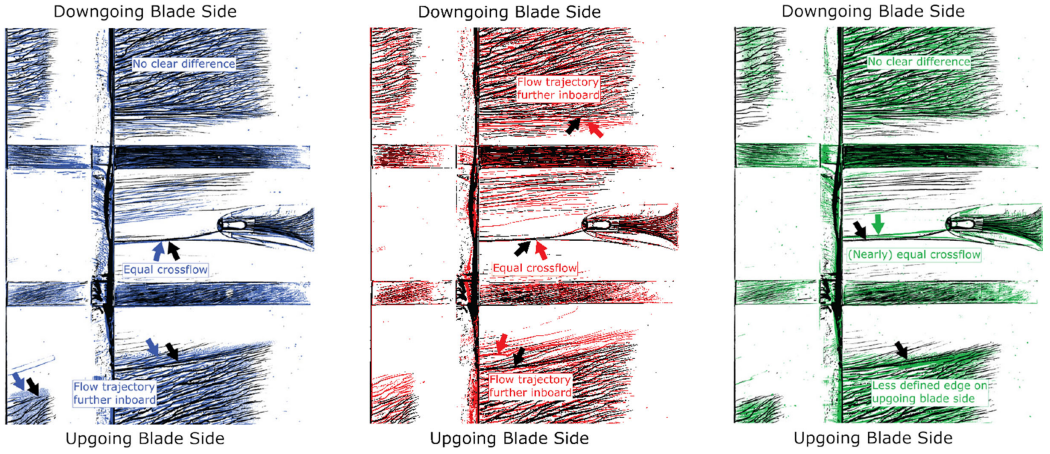

a) High *Tc*/high Q_c (black) versus low *Tc*/high Q_c (blue) **b) High *Tc*/high Q_c (black) versus low *Tc*/low Q_c (red)** **c) High *Tc*/high Q_c (black) versus three-bladed prop (green)**

Fig. 28 Overlays of (zoomed in) processed oil flow images, comparing high-T_c/high-Q_c with each of the other conditions. Lower surface, $\alpha = 8$ deg, $\delta_f = 15$ deg. Freestream from right to left.

the upper surface downgoing blade side and lower surface upgoing blade side. The low-T_c/low-Q_c condition shows less spanwise displacement than the other conditions, with a reduction of roughly $0.15R$ on each of the aforementioned edges. The high-T_c/high-Q_c and low-T_c/high-Q_c conditions result in very comparable slipstream paths, again suggesting that torque coefficient (or longitudinal vorticity in the slipstream) is the dominant parameter for slipstream deformation. Even near the leading edge, the trajectories are nearly equal, indicating that even the leading-edge expansion of the slipstream is hardly affected by T_c (or, rather, azimuthal vorticity in the slipstream).

To further investigate the changes to the internal distribution of total pressure in the slipstream, we combine the various measurement planes of the pressure probe in Fig. 30. It visualizes the development of the various regions of pressure losses. For the high-T_c/high-Q_c condition (Fig. 30a), the regions of total pressure loss are concentrated around a set of vortices. From numerical simulations of the same configuration [10], we know that the central region of total pressure losses is a combination of the viscous core of a nacelle vortex and separation on the blade root at the upgoing blade side. The latter occurs due to the angle of inflow into the propeller, resulting from both the geometric angle with respect to the freestream and the upwash induced by the wing circulation [3,5,29]. The separated blade root wakes wrap around the rolled-up nacelle vortex. This is consistent with the internal distribution of the total pressure coefficient in Fig. 30a.

However, as identified earlier in this section, the various conditions show very different internal distributions of total pressure coefficient. The low-T_c/high-Q_c condition (Fig. 30b) shows no clear vortex cores, despite its similarity in deformation to the high-T_c/high-Q_c condition. Rather, it shows a wide region of lower pressure in the slipstream that stretches along the wing surface. It also lacks the concentration of total pressure at the upgoing blade side that is present in the high-T_c/high-Q_c condition. The low-T_c/low-Q_c condition (Fig. 30c) yields a total pressure distribution that is more comparable to the high-T_c/high-Q_c condition (Fig. 30a) than to the low-T_c/high-Q_c condition (Fig. 30c), while the deformation of the slipstream is much reduced. There is a clear central pressure loss region that originates directly from the nacelle region and a secondary region of total pressure loss, indicating a secondary vortex core, which seems to originate from the wing boundary layer or the nacelle junction. The region of pressure loss around the nacelle

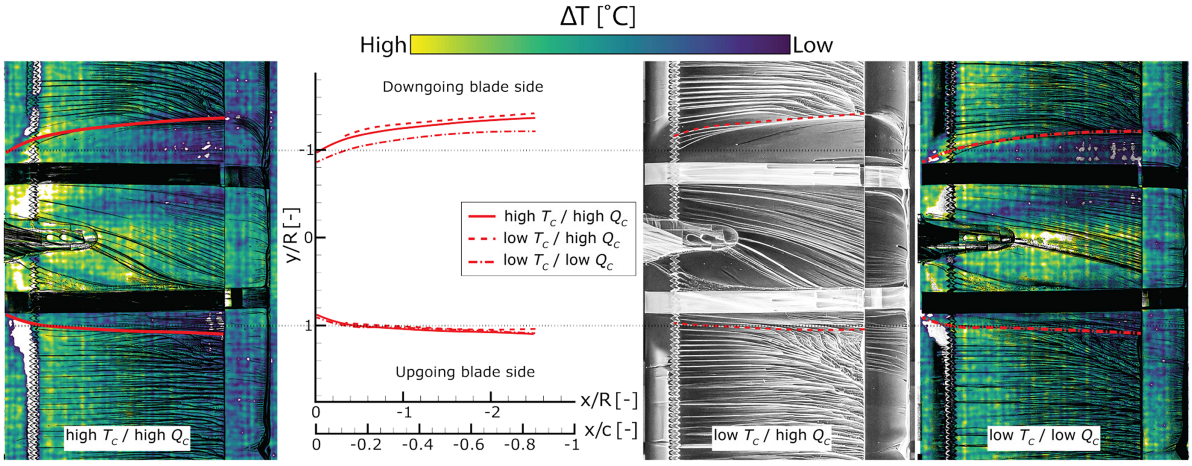

a) Wing upper surface. Oli flow image only. Freestream left to right

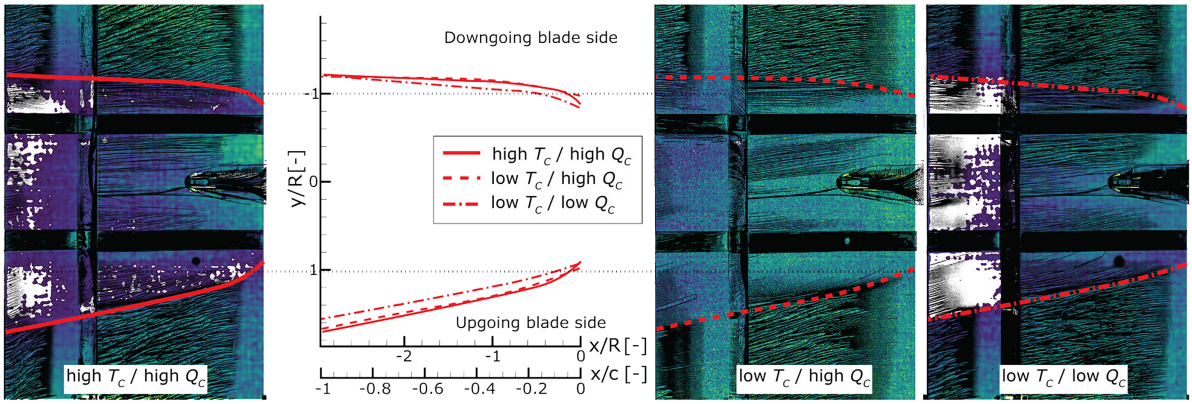

b) Wing lower surface. Freestream right to left

Fig. 29 Comparisons of slipstream edge paths over the wing, estimated from thermography and oil flow visualization. $\alpha = 8$ deg, $\delta_f = 15$ deg.

vortex, which we attributed to separation on the upgoing side blade root, is much increased, however.

The inconsistencies of the internal slipstream distribution between the three conditions and its connection to separation on the upgoing side blade root lead us to conclude that it is not directly related to the values of T_c and Q_c, but rather to the advance ratio. The low-T_c/low-Q_c condition operates at a much higher advance ratio than the high-T_c/high-Q_c condition, and the low-T_c/high-Q_c condition at a higher advance ratio still (see Table 1 in Sec. II). This means that the nonaxial component of inflow imposed on the propeller due to the high-lift condition and angle of attack with respect to the freestream is higher relative to the rotational speed of the propeller. This will induce more separation on the blade root than a lower advance ratio condition but has limited impact on torque and thrust coefficient since it only involves the blade root, where the loading is relatively small. The manner in which the blade root wakes distribute around the slipstream and the wing is highly dependent on the nacelle vortex, however, which is dependent on T_c and Q_c. This results in different internal distributions for each of the tested conditions.

Figure 30 also shows that the various conditions yield different regions of total pressure loss on the wing surface, within the boundaries of the slipstream. These regions are not to be confused with the boundary-layer thickening that occurs just outside the slipstream, which leads to local separation at high angles of attack [8]. The different areas are more clearly shown in Fig. 31, which combines the pressure measurements near the wing surface with the oil flow images. Note that the pressure measurements are positioned at 4 mm from the wing surface, and not all streamlines match exactly with the oil flow visualization. The conditions with high-Q_c show a single region of total pressure loss on the upgoing blade side within the wing-washed area. In the high-T_c/high-Q_c condition (Fig. 31a), this region is separated from the thick wing boundary layer outside the slipstream by a small portion of higher total pressure slipstream flow. In the case of the low-T_c/high-Q_c condition (Fig. 31b), this region merges with the wing boundary layer outside the slipstream near the main element trailing edge. For the low-T_c/low-Q_c condition (Fig. 31c), however, two distinct regions of pressure loss can be identified within the washed area. This likely indicates that for the high-Q_c conditions, these two regions have combined due to the higher crossflow component on the wing surface behind the nacelle.

In previous work [8], the authors have shown that near maximum lift, the region of pressure loss within the washed area can cause local separation and even merge with flow separation zones outside the slipstream. Figure 31 clearly shows that the regions of pressure losses originate from the nacelle region. For the low-T_c/low-Q_c condition (Fig. 31c), the two regions can be traced to the nacelle–wing junction on either side of the nacelle. At these junctions, separation bubbles can occur as the rapidly accelerating flow around the leading edge meets the flow passing along the nacelle [5,8]. These bubbles are strongest at the upgoing blade side, where the acceleration around the leading edge is largest as a result of the increased angle of attack induced by the local tangential velocities in the slipstream. This may be directly related to the observed pressure regions, of which the region originating from the upgoing blade side junction has the most significant total pressure losses, as well as the secondary vortex observed in Fig. 30c. The nacelle integration clearly has an important role in the propeller–wing interaction in high-lift configurations.

IV. Conclusions

In this paper, we have shown how the deformation of the slipstream due to wing interaction is related to the operating condition of the propeller, specifically the thrust and torque coefficients.

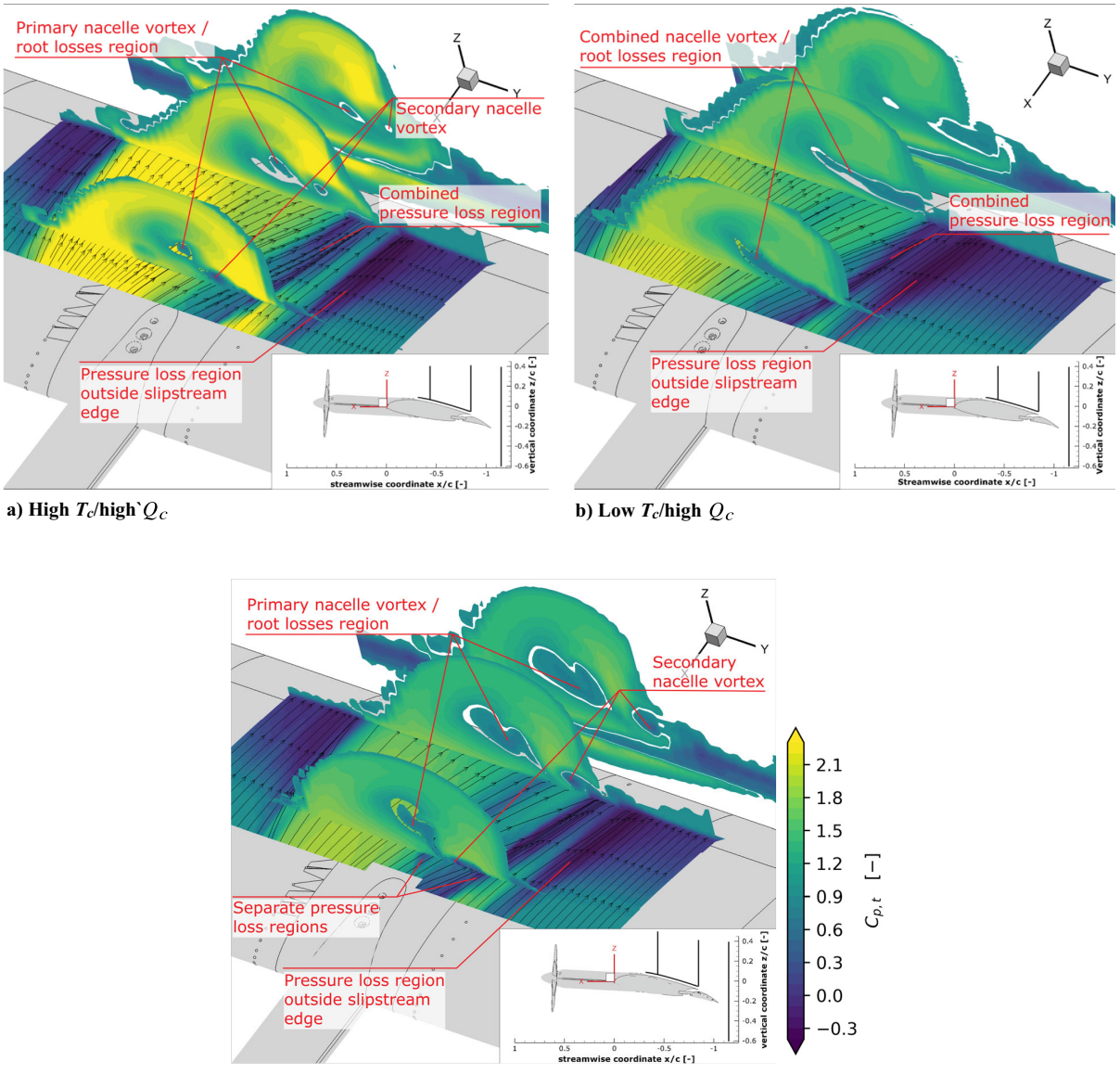

a) High T_c/high`Q_c

b) Low T_c/high Q_c

c) Low T_c/low Q_c

Fig. 30 Distributions of $C_{p,t}$ at various chordwise slices and the surface plane, showing development of the nacelle vortex and pressure loss regions in the slipstream. $\alpha = 8$ deg, $\delta_f = 15$ deg.

We used seven-hole pressure probe measurements, oil flow visualization, and IR thermography to compare three main conditions of the propeller: a baseline condition, a condition with a comparable torque coefficient but a much lower thrust coefficient, and a condition where both thrust and torque are significantly lower than the baseline. A fourth condition included the same thrust and torque coefficient as the baseline but with a reduced number of blades. Unfortunately, this condition suffered from blade tip separation, limiting the reliability of the results. We have compared the impact of each of these conditions on the slipstream–wing aerodynamic interaction in both low-lift and high-lift configurations. The full dataset of the experiment is available for future numerical validation.

This paper includes several conclusions regarding the dependency of slipstream deformation due to propeller–wing aerodynamic interaction on the operating characteristics of the propeller:

1) Torque coefficient, or longitudinal vorticity in the slipstream, is the dominant parameter for the slipstream deformation.

2) A lower torque coefficient leads to significantly lower crossflow components on the wing surface directly behind the nacelle and also results in less spanwise displacement of the slipstream edge on the wing surface.

3) Thrust coefficient, or azimuthal vorticity in the slipstream, has a negligible impact on the deformation of the slipstream.

4) The impact of propeller condition on the slipstream deformation and development is much larger in high-lift configuration than in low-lift configuration. Whereas in low lift the propeller condition mostly impacts the displacement near the wing surface, in high lift it affects both the internal distribution of total pressure and the slipstream shape further away from the wing surface.

5) The nacelle integration has a major impact on the internal distribution of total pressure in the slipstream, as well as on local pressure loss regions on the wing surface.

Further research is required to understand the deformation of the slipstream at the leading edge in high-lift configuration, which seems to be dominating the downstream development. The data obtained in this region during the experiment described in this paper is limited. This will likely require instantaneous flow measurements that can identify the individual tip vortices or high-fidelity numerical simulations. Additionally, the findings in this paper again stress the importance of nacelle integration in the propeller–wing interaction problem. Both the vertical position of the slipstream relative to the wing chord and the physical junctions between the wing and nacelle have dominant effects on the

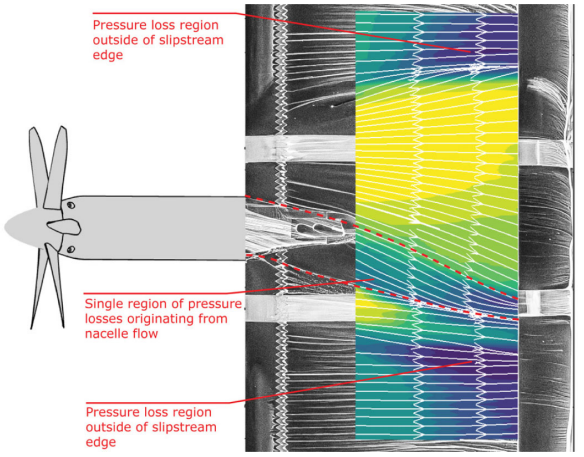

a) High T_c/high Q_c

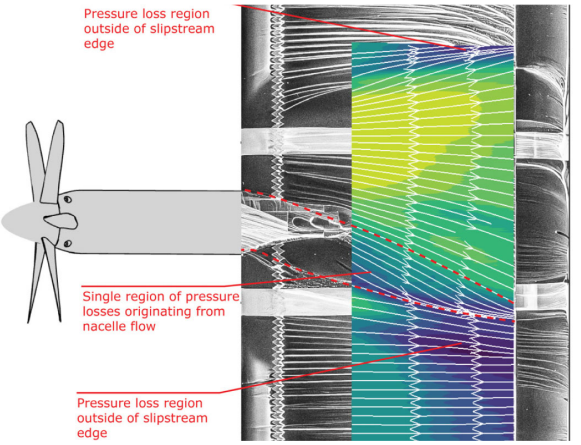

b) Low T_c/high Q_c

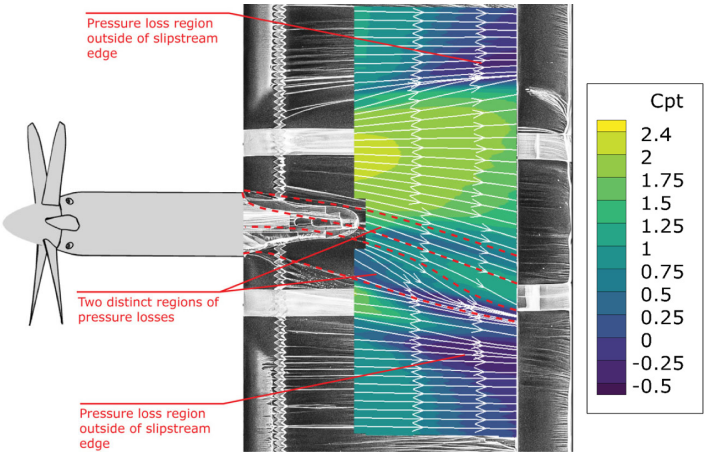

c) Low T_c/low Q_c

Fig. 31 Contours of $C_{p,t}$ at 4 mm from the surface, and oil flow visualization on the wing surface, showing the pressure loss regions in the slipstream. $\alpha = 8$ deg, $\delta_f = 15$ deg.

slipstream deformation and how the wing flow is impacted by the propeller slipstream.

Acknowledgments

This work is partially funded by the Deutsche Forschungsgemeinschaft (DFG, German Research Foundation) under Germany's Excellence Strategy—EXC 2163/1—Sustainable and Energy Efficient Aviation—Project-ID 390881007. The authors would like to thank everyone who assisted in the execution of the experiment, in particular Fernanda do Nascimento Monteiro for her continued assistance. Special thanks are also in order for Stephan Bernardy, Emiel Langedijk, and Martijn Looman for their technical support and quick problem-solving. Additional thanks to Daamanjyot Barara for providing the propeller performance simulations that were the basis of the test matrix selection.

References

[1] Witkowski, D. P., Lee, A. K., and Sullivan, J. P., "Aerodynamic Interaction Between Propellers and Wings," *Journal of Aircraft*, Vol. 26, No. 9, 1989, pp. 829–836. https://doi.org/10.2514/3.45848

[2] Jameson, A., "The Analysis of Propeller-Wing Flow Interaction," *NASA SP-228: Analytic Methods in Aircraft Aerodynamics*, 1970, pp. 721–742.

[3] Veldhuis, L., "Propeller Wing Aerodynamic Interference," Ph.D. Dissertation, Delft Univ. of Technology, Delft, The Netherlands, 2005.

[4] Sinnige, T., "Aerodynamic and Aeroacoustic Interaction Effects for Tip-Mounted Propellers - An Experimental Study," Ph.D. Dissertation, Delft Univ. of Technology, Delft, The Netherlands, 2018. https://doi.org/10.4233/uuid:214e1e9a-c53e-47c7-a12c-b1eb3ec8293b.

[5] van Arnhem, N., "Unconventional Propeller-Airframe Integration for Transport Aircraft Configurations," Ph.D. Dissertation, Delft Univ. of Technology, Delft, The Netherlands, 2022. https://doi.org/10.4233/uuid:4d47b0db-1e6a-4f38-af95-aafd33c29402 Publication

[6] de Vries, R., "Hybrid-Electric Aircraft with Over-the-Wing Distributed Propulsion Aerodynamic Performance and Conceptual Design," Ph.D. Dissertation, Delft Univ. of Technology, Delft, The Netherlands, 2022. https://doi.org/10.4233/uuid:ef87dc11-e7b2-4726-a41f-28588d64c58d

[7] Felli, M., "Underlying Mechanisms of Propeller Wake Interaction with a Wing," *Journal of Fluid Mechanics*, Vol. 908, 2021, Paper A10. https://doi.org/10.1017/jfm.2020.792

[8] Duivenvoorden, R. R., Suard, N., Sinnige, T., and Veldhuis, L. L., "Experimental Investigation of Aerodynamic Interactions of a Wing with Deployed Fowler Flap Under Influence of a Propeller Slipstream," *AIAA AVIATION 2022 Forum*, AIAA Paper 2022-3216, 2022. https://doi.org/10.2514/6.2022-3216

[9] Duivenvoorden, R., Sinnige, T., and Veldhuis, L., "Experimental Dataset of a Single Propeller-Wing-Flap Model (TUD-PWF) at Various Flap Deflections, Angles of Attack and Propeller Conditions," 4TU.ResearchData, April 2025. https://doi.org/10.4121/3161B813-AD38-4F9C-BB9D-333B895F46BC.V1

[10] Ribeiro, A. F., Duivenvoorden, R., and Martins, D., "High-Fidelity Simulations of Propeller-Wing Interactions in High-Lift Conditions," *AIAA AVIATION 2023 Forum*, AIAA Paper 2023-3541, 2023. https://doi.org/10.2514/6.2023-3541

[11] Duivenvoorden, R. R., Monteiro, F. N., and Sinnige, T., "Experimental Measurements of Slipstream Deformation for an Installed Distributed Propeller Configuration," *34th Congress of the International Council*

of the Aeronautical Sciences, International Council of the Aeronautical Sciences, Florence, Italy, 2024, pp. 1–12.

[12] Barker, J. E., Zarri, A., Christophe, J., and Schram, C. F., "Numerical Investigation of Tonal Noise Emissions from Propeller-Wing Aerodynamic and Acoustic Interactions," *AIAA AVIATION Forum*, AIAA Paper 2023-4056, 2023. https://doi.org/10.2514/6.2023-4056

[13] Monteiro, F.d, Duivenvoorden, R., Ragni, D., Avallone, F., and Sinnige, T., "Experimental Analysis of Synchrophasing Impact on Noise of Distributed Propeller Systems in Tractor Configuration," *30th AIAA/CEAS Aeroacoustics Conference*, AIAA Paper 2024-3421, 2024. https://doi.org/10.2514/6.2024-3421

[14] Yang, Z., Meinke, M., and Schroeder, W., "Numerical Analysis of Propeller-Airfoil Interaction in a Distributed Propulsion System Using a Hybrid LES and FW-H Approach," *30th AIAA/CEAS Aeroacoustics Conference*, AIAA Paper 2024-3211, 2024. https://doi.org/10.2514/6.2024-3211

[15] Boermans, L., and Rutten, P., "Two-Dimensional Aerodynamic Characteristics of Airfoil NLF-MOD22 with Fowler Flap," Delft Univ. of Technology TR LSW-95-3, Delft, The Netherlands, 1995.

[16] Duivenvoorden, R. R., Sinnige, T., and Veldhuis, L. L., "TU Delft Propeller-Wing-Flap (TUD-PWF) Wind Tunnel Model Geometry," AIAA Paper 2022-3216, 2025. https://doi.org/10.2514/6.2022-3216

[17] de Vries, R., van Arnhem, N., Sinnige, T., Vos, R., and Veldhuis, L. L., "Aerodynamic Interaction Between Propellers of a Distributed-Propulsion System in Forward Flight," *Aerospace Science and Technology*, Vol. 118, Nov. 2021, Paper 107009. https://doi.org/10.1016/j.ast.2021.107009

[18] van Arnhem, N., de Vries, R., Sinnige, T., and Veldhuis, L. L., "XPROP-S Propeller Geometry," *Zenodo*, 2022. https://doi.org/10.5281/zenodo.6355670

[19] Dobbinga, E., and van Ghesel Grothe, J. A., "De Lage-Snelheids Windtunnel Van De Sub-Afdeling Vliegtuig Bouwkunde Der Technische Hogeschool," Delft Univ. of Technology TR 77, 1955, https://resolver.tudelft.nl/uuid:dbf0b1e4-f765-439f-9acd-309de527d2c7.

[20] Serpieri, J., "Cross-Flow Instability: Flow Diagnostics and Control of Swept Wing Boundary Layers," Ph.D. Dissertation, Delft Univ. of Technology, Delft, The Netherlands, 2018. https://doi.org/10.4233/uuid:3dac1e78-fcc3-437f-9579-048b74439f55.

[21] Barlow, J. B., Rae, W. H., and Pope, A., *Low-Speed Wind Tunnel Testing*, 3rd ed., Wiley, New York, 1999, p. 352.

[22] Savitzky, A., and Golay, M. J. E., "Smoothing and Differentiation of Data by Simplified Least Squares Procedures," *Analytical Chemistry*, Vol. 36, No. 8, 1964, pp. 1627–1639. https://doi.org/10.1021/ac60214a047

[23] Shaw-ward, S., Titchmarsh, A., and Birch, D. M., "Calibration and Use of n-Hole Velocity Probes," *AIAA Journal*, Vol. 53, No. 2, 2015, pp. 336–346. https://doi.org/10.2514/1.J053130

[24] Zuccher, S., and Saric, W. S., "Infrared Thermography Investigations in Transitional Supersonic Boundary Layers," *Experiments in Fluids*, Vol. 44, No. 1, 2007, pp. 145–157. https://doi.org/10.1007/s00348-007-0384-1

[25] Simon, B., Filius, A., Tropea, C., and Grundmann, S., "IR Thermography for Dynamic Detection of Laminar-Turbulent Transition," *Experiments in Fluids*, Vol. 57, No. 5, 2016, p. 93. https://doi.org/10.1007/s00348-016-2178-9

[26] Lötstedt, P., "A Propeller Slipstream Model in Subsonic Linearized Potential Flow," *17th Congress of the International Council of Aerospace Sciences*, ICAS-90-5.4.4 ICAS-90-5.4.4, International Council of the Aeronautical Sciences, 1990, pp. 733–744

[27] van Arnhem, N., de Vries, R., Sinnige, T., Vos, R., Eitelberg, G., and Veldhuis, L. L. M., "Engineering Method to Estimate the Blade Loading of Propellers in Nonuniform Flow," *AIAA Journal*, Vol. 58, No. 12, 2020, pp. 5332–5346. https://doi.org/10.2514/1.J059485

[28] Öhman, L. H., "Torque and Thrust from Five-Hole Pressure Probe Measurements in the Near Slipstream of a Propeller in Compressible Flow," National Research Council Canada IAR-AN-81, Ottawa, Canada, 1995.

[29] Stokkermans, T. C. A., and Veldhuis, L. L. M., "Propeller Performance at Large Angle of Attack Applicable to Compound Helicopters," *AIAA Journal*, Vol. 59, No. 6, 2021, pp. 2183–2199. https://doi.org/10.2514/1.J059509

A. Jones
Associate Editor